Journal of
Applied Crystallography
ISSN 0021-8898
Editor: **Anke R. Kaysser-Pyzalla**

Inferential statistics of electron backscatter diffraction data from within individual crystalline grains

Florian Bachmann, Ralf Hielscher, Peter E. Jupp, Wolfgang Pantleon, Helmut Schaeben and Elias Wegert

J. Appl. Cryst. (2010). **43**, 1338–1355

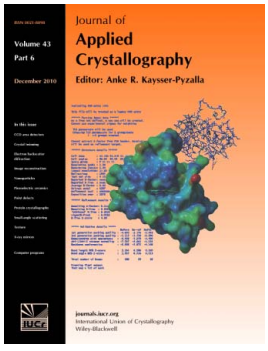

Journal of
Applied
Crystallography
ISSN 0021-8898

Received 4 April 2010
Accepted 29 July 2010

Inferential statistics of electron backscatter diffraction data from within individual crystalline grains

Florian Bachmann,[a] Ralf Hielscher,[b] Peter E. Jupp,[c] Wolfgang Pantleon,[d] Helmut Schaeben[a]* and Elias Wegert[e]

[a]Geoscience Mathematics and Informatics, TU Bergakademie Freiberg, Germany, [b]Applied Functional Analysis, TU Chemnitz, Germany, [c]School of Mathematics and Statistics, University of St Andrews, Fife, Scotland, [d]Center for Fundamental Research, Metal Structures in Four Dimensions, Risø National Laboratory for Sustainable Energy, Materials Research Division, Technical University of Denmark, Roskilde, Denmark, and [e]Applied Analysis, TU Bergakademie Freiberg, Germany. Correspondence e-mail: schaeben@geo.tu-freiberg.de

Highly concentrated distributed crystallographic orientation measurements within individual crystalline grains are analysed by means of ordinary statistics neglecting their spatial reference. Since crystallographic orientations are modelled as left cosets of a given subgroup of SO(3), the non-spatial statistical analysis adapts ideas borrowed from the Bingham quaternion distribution on $\mathbb{S}^3$. Special emphasis is put on the mathematical definition and the numerical determination of a 'mean orientation' characterizing the crystallographic grain as well as on distinguishing several types of symmetry of the orientation distribution with respect to the mean orientation, like spherical, prolate or oblate symmetry. Applications to simulated as well as to experimental data are presented. All computations have been done with the free and open-source texture toolbox *MTEX*.

1. Introduction and motivation

The subject of this communication is the non-spatial statistical analysis of highly concentrated crystallographic orientations measured within individual crystallographic grains. Crystallographic orientations are explicitly considered as left cosets of crystallographic symmetry groups, *i.e.* classes of crystallographically symmetrically equivalent rotations. Our objective is twofold.

Primarily, this work is an attempt to clarify a lasting confusion concerning the 'mean orientation' characterizing a grain, *i.e.* its mathematical definition and its numerical determination (Humbert *et al.*, 1996; Morawiec, 1998; Barton & Dawson, 2001*a*,*b*; Glez & Driver, 2001; Humphreys *et al.*, 2001; Pantleon, 2005; Cho *et al.*, 2005; He *et al.*, 2008; Krog-Pedersen *et al.*, 2009; Pantleon *et al.*, 2008), and then to proceed to its meaning for inferential statistics.

The second objective is to verify these theoretical findings with fabricated and experimental data from within individual grains. Our approach here is diametrically different to the more commonly used approach in electron backscatter diffraction (EBSD) to the misorientation within individual grains, which seeks to explain the orientation gradients in terms of dislocation slip systems using the Nye tensor (El-Dasher *et al.*, 2003; Field *et al.*, 2005; Nye, 1953; Pantleon, 2008; Wheeler *et al.*, 2009; Wilkinson *et al.*, 2006).

For all computations we use the versatile features of the free and open-source *Matlab* (MathWorks, Natick, MA, USA) software toolbox *MTEX* (Hielscher, 2007; Hielscher & Schaeben, 2008; Schaeben *et al.*, 2007), providing a unifying approach to texture analysis with individual ('EBSD') or integral ('pole figure') orientation measurements. For the time being, the functions implemented in *MTEX* require the assumption that the rotation or orientation measurements are independent even if they are spatially indexed and likely to be spatially dependent. Whenever this artificial assumption is essential, it is made explicit. Readers are referred to van den Boogaart (1999, 2002) for fundamental spatial statistics of orientations, and to forthcoming publications reporting the additional implementation of functions in *MTEX* to apply spatial statistics numerically.

The next section provides preliminaries concerning quaternions, notions of descriptive spherical statistics, and the relationship of individual orientation measurements and left cosets of some rotational subgroups induced by crystallographic symmetry, *i.e.* classes of rotations equivalent by crystallographic symmetry, which cannot be distinguished physically but should be distinguished mathematically. The third section applies the Bingham quaternion distribution to highly concentrated individual orientation measurements as sampled, *e.g.*, by EBSD. In particular, it is shown that quaternion multiplication of the measurements by a given reference orientation acts analogously to centring the measurements with respect to this reference orientation. Therefore, replacing the initial orientation measurements by

their corresponding disorientations, *i.e.* orientation differences with respect to the reference orientation, is obsolete. The orientation tensor derived from the initial measurements contains all ingredients necessary for the characterization of details of the highly concentrated distribution of orientations. The final section completes this communication with practical examples of simulated and experimental EBSD data sets.

2. Preliminaries

2.1. Quaternions

The group SO(3) may be considered in terms of $\mathbb{H}$, the skew field of real quaternions. In particular, a unit quaternion $q \in \mathbb{S}^3 \subset \mathbb{H}$ determines a rotation. For unit quaternions the inverse equals the conjugate, $q^{-1} = q^*$. The unit quaternion q and its negative $-q$ describe the same rotation. Thus, it would make sense to identify the pair $(q, -q)$ with a unique rotation. Working with pairs may be quite cumbersome; for general statistical purposes the proper entity to work with is the (4×4) symmetric matrix

$$Q = \begin{pmatrix} q_1^2 & q_1q_2 & q_1q_3 & q_1q_4 \\ q_1q_2 & q_2^2 & q_2q_3 & q_2q_4 \\ q_1q_3 & q_2q_3 & q_3^2 & q_3q_4 \\ q_1q_4 & q_2q_4 & q_3q_4 & q_4^2 \end{pmatrix}. \tag{1}$$

Thinking of $q = (q_1, q_2, q_3, q_4)^{\mathsf{T}}$ as elements of $\mathbb{S}^3 \subset \mathbb{R}^4$ we could write $Q = qq^{\mathsf{T}}$.

The product of two quaternions is defined as

$$\begin{aligned} pq = {} & \mathrm{Sc}(p)\mathrm{Sc}(q) - \mathrm{Vec}(p) \cdot \mathrm{Vec}(q) \\ & + \mathrm{Sc}(p)\mathrm{Vec}(q) + \mathrm{Sc}(q)\mathrm{Vec}(p) + \mathrm{Vec}(p) \cdot \mathrm{Vec}(q), \end{aligned} \tag{2}$$

where $\mathrm{Sc}(p)$ and $\mathrm{Vec}(p)$ denote the scalar and vector part of the quaternion p, respectively. The quaternion product can be rewritten as

$$pq = L_p q = \begin{pmatrix} p_0 & -p_1 & -p_2 & -p_3 \\ p_1 & p_0 & -p_3 & p_2 \\ p_2 & p_3 & p_0 & -p_1 \\ p_3 & -p_2 & p_1 & p_0 \end{pmatrix} q, \tag{3}$$

and analogously

$$qp = R_p q = \begin{pmatrix} p_0 & -p_1 & -p_2 & -p_3 \\ p_1 & p_0 & p_3 & -p_2 \\ p_2 & -p_3 & p_0 & p_1 \\ p_3 & p_2 & -p_1 & p_0 \end{pmatrix} q, \tag{4}$$

where the matrices L_p and R_p, respectively, have the properties

$$\begin{aligned} & L_{p^*} = L_p^{\mathsf{T}}, \quad R_{p^*} = R_p^{\mathsf{T}}, \\ & L_{p^*}L_p = L_{p^*p} = L_1 = E, \\ & R_{p^*}R_p = R_{pp^*} = R_1 = E, \end{aligned} \tag{5}$$

i.e. they are orthonormal (*cf.* Gürlebeck *et al.*, 2006, p. 33).

The scalar product of two quaternions is defined as

$$p \cdot q = \mathrm{Sc}(pq^*) = \mathrm{Sc}(p)\mathrm{Sc}(q) + \mathrm{Vec}(p) \cdot \mathrm{Vec}(q) = \cos \measuredangle(p, q). \tag{6}$$

The scalar product of the unit quaternions p and q agrees with the inner (scalar) product of p and q when recognized as elements of $\mathbb{S}^3 \subset \mathbb{R}^4$, *i.e.* the scalar product provides the canonical measure for the distance of unit quaternions (*cf.* Gürlebeck *et al.*, 2006, p. 21).

2.2. Descriptive spherical statistics

Even though spherical statistics is not the topic here, the entities considered are borrowed from spherical statistics (Watson, 1983; Mardia & Jupp, 2000). The following issues have been clarified in the context of texture analysis by Morawiec (1998).

In spherical statistics a distinction is made between vectors q and pairs $(q, -q)$ of antipodal vectors, *i.e.* axes.

2.2.1. Vectorial data. The key summary statistic of vectorial data is the normalized sample mean vector

$$r = \frac{1}{\| \sum_{\ell=1}^n q_\ell \|} \sum_{\ell=1}^n q_\ell, \tag{7}$$

where r provides a measure of location and $\| \sum q_\ell \|$ provides a measure of dispersion (concentration). The normalized mean vector solves the following minimization problem. Given vectorial data $q_1, \ldots, q_n \in \mathbb{S}^3 \subset \mathbb{R}^4$ find $r \in \mathbb{S}^3$ minimizing the 'mean angular' deviation. More precisely, with $\theta_\ell = \measuredangle(q_\ell, x)$ the entity to be minimized is

$$\begin{aligned} F_R(x; q_1, \ldots, q_n) &= \frac{1}{n}\sum_{\ell=1}^n (1 - \cos\theta_\ell) = 1 - \frac{1}{n}\sum_{\ell=1}^n \cos\theta_\ell \\ &= 1 - \frac{1}{n}\sum_{\ell=1}^n x q_\ell = 1 - x\left(\frac{1}{n}\sum_{\ell=1}^n q_\ell\right) = 1 - x\overline{q}. \end{aligned} \tag{8}$$

Thus, the solution $x_0 = r$ is provided by the normalized mean vector

$$r = \frac{\overline{q}}{\|\overline{q}\|}, \tag{9}$$

and

$$F_R(r; q_1, \ldots, q_n) = 1 - \|\overline{q}\| \tag{10}$$

is a measure for the spherical dispersion of the data. The normalized mean vector is also the solution of the problem of minimizing the sum of squared Euclidean distances as

$$\begin{aligned} \frac{1}{n}\sum_{\ell=1}^n \|q_\ell - x\|^2 &= \frac{1}{n}\sum_{\ell=1}^n (q_\ell - x)(q_\ell - x) = \frac{1}{n}\sum_{\ell=1}^n (2 - 2\cos\theta_\ell) \\ &= 2F_R(x; q_1, \ldots, q_n) \end{aligned} \tag{11}$$

(Humbert *et al.*, 1996). However, the normalized mean vector does not provide statistical insight into a sample of quaternions used to parametrize rotations (Watson, 1983; Mardia & Jupp, 2000, §13.2.1).

2.2.2. Axial data. The key summary statistic of axial data is the orientation tensor

$$T = \frac{1}{n}\sum_{\ell=1}^n q_\ell q_\ell^{\mathsf{T}}. \tag{12}$$

Its spectral decomposition into the set of eigenvectors $a_1, \ldots, a_4$ and the set of corresponding eigenvalues $\lambda_1, \ldots, \lambda_4$ provides a measure of location and a corresponding measure of dispersion, respectively. Since the orientation tensor T and the tensor of inertia I are related by

$$I = E - T, \tag{13}$$

where E denotes the unit matrix, the eigenvectors of T provide the principal axes of inertia and the eigenvalues of T provide the principal moments of inertia. From the definition of T as a quadratic form, T is positive definite, implying that all eigenvalues are real and non-negative; moreover, they sum to 1.

The spectral decomposition solves the following minimization problem. Given axial data $q_1, \ldots, q_n \in \mathbb{S}^3$ find $a \in \mathbb{S}^3$ minimizing the mean squared orthogonal distance. With $\theta_\ell = \measuredangle(q_\ell, x)$ as before, the entity to be minimized is

$$\begin{aligned} F_T(x; q_1, \ldots, q_n) &= \frac{1}{n}\sum_{\ell=1}^{n} \sin^2\theta_\ell = \frac{1}{n}\sum_{\ell=1}^{n}\left(1 - \cos^2\theta_\ell\right) \\ &= 1 - \frac{1}{n}\sum \cos^2\theta_\ell = 1 - \frac{1}{n}\sum_{\ell=1}^{n}(x^{\mathsf{T}} q_\ell)^2 \\ &= 1 - x^{\mathsf{T}}\left(\frac{1}{n}\sum_{\ell=1}^{n} q_\ell q_\ell^{\mathsf{T}}\right)x \\ &= 1 - x^{\mathsf{T}} T x. \end{aligned} \tag{14}$$

Obviously, the solution $x_0 = a_1$ is provided by the eigenvector a_1 of T corresponding to the largest eigenvalue denoted λ_1. Then $1 - \lambda_1$ is a measure of the spherical dispersion of the axial data with respect to the quaternion $\pm a_1$. The eigenvalues are related to the shape parameters of the Bingham (quaternion) distribution (Bingham, 1964, 1974; Kunze & Schaeben, 2004, 2005) by a system of algebraic equations involving partial derivatives of the hypergeometric function ${}_1F_1$ of a (4×4) matrix argument.

In general, a single eigenvector and its eigenvalue are insufficient to provide a reasonable characterization of the data. Therefore, often the ratios of the eigenvalues are analysed and interpreted.

2.2.3. Normalized mean vector *versus* first principal axis of inertia. It is emphasized that the mean vector for axial data is always identically zero. Despite this mathematical fact, it may sometimes be tempting to treat axes like vectors. If axes are treated as vectors by some 'trick', *e.g.* moving all data to the 'upper hemisphere', the statistical inference will generally be misleading. A uniform distribution on the upper hemisphere will appear as preferred distribution in terms of vectors, but as uniform distribution in terms of axes.

In the special case of a highly preferred unimodal distribution of axes, and after additional provision as sketched above, the normalized mean vector may be a sufficiently good approximation to the eigenvector corresponding to the largest eigenvector. This approximation may be considered sufficiently good as long as cos is considered as a sufficiently good approximation to $\cos^2$, *i.e.* for (very) small angles.

In the case of highly unimodal preferred orientation, the largest eigenvalue λ_1 is much larger than the other eigenvalues and provides a first measure of the dispersion just by itself. The other eigenvalues and their ratios provide insight into the shape of the distribution, *e.g.* the extent to which it is symmetrical or not.

This special case seems to apply to individual orientation measurements within a crystalline grain, where the EBSD measurements should differ only very little. However, careful attention should be paid to the way of defining individual grains, *i.e.* to the way of defining grain boundaries. A common practice in defining the boundaries of grains is based on a measurement-by-measurement comparison of orientations, *i.e.* two measurements $q_0 = q(x)$ and $q_1 = q(x + \delta x)$ located next to one another (separated by a grid step of size δx) are compared. If the orientation difference is smaller than a user-defined threshold ω_0, the two positions $x, x + \delta x$ are assigned to the same grain. Then $q_1 = q(x + \delta x)$ and $q_2 = q(x + 2\delta x)$ are compared. If the orientation difference is larger than the threshold, a grain boundary is constructed (*e.g.* Lloyd *et al.*, 1997; Heilbronner, 2000).

Determined in this way the size and the shape of a crystallographic grain depend rather on the threshold ω_0 defined by the user than on the amount of available sampling controlled by the grid step size δx. Thus, a grain is referred to as a definition – rather than a sampling-limited spatial object (*cf.* Bonham-Carter, 1996, p. 29–30). Then the orientation gradient along the line $x, x + m\,\delta x$, $m \in \mathbb{N}$, may be large enough to result occasionally in surprisingly large dispersions which may be prohibitive of any reasonable interpretation in terms of 'grain' properties or prevent a simple comparison of 'grains' defined in this way.

2.3. Considering crystallographic symmetry

In the case of crystallographic symmetry $G_{\text{Laue}} \cap \mathbb{S}^3 = \tilde{G}_{\text{Laue}} \subset \mathbb{S}^3$ to be considered in terms of the restriction $\tilde{G}_{\text{Laue}}$ of the Laue group G_{Laue} to rotations, an additional difficulty has to be mastered, as crystal orientations that are equivalent under crystal symmetries must be considered to determine a mean orientation. In fact, the initial orientation measurements are of the form $q_\ell g_{m_\ell}$, $q_\ell \in \mathbb{S}^3$, $g_{m_\ell} \in \tilde{G}_{\text{Laue}}$, *i.e.* they are some elements of the corresponding left cosets $q_\ell \tilde{G}_{\text{Laue}}$.

If q_i and q_j are very close, $q_i g_1$ and $q_j g_2$, $g_1, g_2 \in \tilde{G}_{\text{Laue}}$, $g_1 \neq g_2$, may appear to be mathematically different though they are physically close. The practical problem with the computation of the orientation tensor T and its spectral decomposition, respectively, is to transform the initial elements of the sample such that they are not only physically but also mathematically highly concentrated.

Thus, explicitly considering crystallographic symmetry, the entity to be minimized [*cf.* equation (14)] actually is

$$F_T(x; q_1, \ldots, q_n, \tilde{G}_{\text{Laue}}) = 1 - x^{\mathsf{T}}\left[\frac{1}{n}\sum_{\ell=1}^{n}(q_\ell \tilde{G}_{\text{Laue}})(q_\ell \tilde{G}_{\text{Laue}})^{\mathsf{T}}\right]x \tag{15}$$

given crystallographic orientations $q_1, \ldots, q_n$, and the rotational symmetry group $\tilde{G}_{\rm Laue}$, *i.e.*

$$\operatorname{argmin}_{x\in\mathbb{S}^3, g_{m_\ell}\in\tilde{G}_{\rm Laue}} \left\{1 - x^{\mathsf{T}}\left[\frac{1}{n}\sum_{\ell=1}^{n}(q_\ell g_{m_\ell})(q_\ell g_{m_\ell})^{\mathsf{T}}\right]x\right\} \quad (16)$$

with $g_{m_\ell} \in \tilde{G}_{\rm Laue}, m_\ell = 1, \ldots, s,\ \ell = 1, \ldots, n,$ where s denotes the cardinality of $\tilde{G}_{\rm Laue}$.

While the map $\mathbb{S}^3 \rightarrow \mathbb{S}^3/\tilde{G}_{\rm Laue}$ is continuous, its inverse is not. Thus, assigning to each measured orientation $q_\ell g_{m_\ell}$ the element of $q_\ell \tilde{G}_{\rm Laue}$ with the smallest angle of rotation does not lead to a solution of equation (16).

Therefore, we apply the following heuristics to resolve the problem of equation (16). To this end, an initial reference orientation is required. Given the data set $q_1, \ldots, q_n$, we may choose q_1 as reference orientation. For every $\ell = 1, \ldots, n$, determine $\operatorname{argmax}_{g\in\tilde{G}_{\rm Laue}} q_\ell g \times q_1 = g_{0,\ell}^{(0)} \in \tilde{G}_{\rm Laue}$ and replace q_ℓ by $q_\ell^{(0)} = q_\ell g_{0,\ell}^{(0)}$. Then we evaluate $F_T[x; q_1^{(0)}, \ldots, q_n^{(0)}]$ for determining the largest eigenvalue $\lambda_1^{(0)}$ and its corresponding eigenvector $a_1^{(0)}$.

Then we choose $a_1^{(0)}$ as the reference orientation, determine for every $\ell = 1, \ldots, n$, $\operatorname{argmax}_{g\in\tilde{G}_{\rm Laue}} q_\ell^{(0)} g \times a_1^{(0)} = g_{0,\ell}^{(1)} \in \tilde{G}_{\rm Laue}$, and replace $q_\ell^{(0)}$ by $q_\ell^{(1)} = q_\ell^{(0)} g_{0,\ell}^{(1)}$. Then we evaluate $F_T[x; q_1^{(1)}, \ldots, q_n^{(1)}]$ for determining the largest eigenvalue $\lambda_1^{(1)}$ and its corresponding eigenvector $a_1^{(1)}$.

Now let $i = 1, \ldots, I$ enumerate the successive iterations. For every $\ell = 1, \ldots, n$, we replace $q_\ell^{(i-1)}$ by $q_\ell^{(i)}$. Next we evaluate $F_T[x; q_1^{(i)}, \ldots, q_n^{(i)}]$, and determine the largest eigenvalue $\lambda_1^{(i)}$ and its corresponding eigenvector $a_1^{(i)}$, which will be the reference orientation in the next step of this iterative approximation. We continue until $\lambda_1^{(i)}$ does not increase any longer and its corresponding eigenvector $a_1^{(i)}$ does not change any more.

This iterative procedure to determine the proper eigenvector corresponding to the largest eigenvalue is similar to the one suggested by Pantleon (2005), Pantleon *et al.* (2008), He *et al.* (2008) and Krog-Pedersen *et al.* (2009) to be applied to the normalized mean vector. It converges only if the measurements are sufficiently well clustered, *i.e.* if their dispersion is sufficiently small, and if it is appropriately initialized. The modal orientation, *i.e.* the orientation for which the kernel-estimated orientation density function is maximum, may be a more appropriate initial reference orientation than an arbitrary measured orientation.

3. Characterizing sets of highly preferred orientation

Neglecting this problem of how to define grains and their boundaries, the confusion about the normalized mean vector and the spectral decomposition can be avoided if it is assumed that (*a*) the measurements $q_1, \ldots, q_n$ are highly preferred, *i.e.* the dispersion within an individual grain is small, and (*b*) a mean orientation a_1 has been assigned to the grain by means of the eigenvector a_1 corresponding to the largest eigenvector λ_1 according to equation (14), which has been interpreted itself as a measure of the extent of preferred orientation, *i.e.* (λ_1, a_1) are no longer the statistics of primary interest.

Then the focus is on (λ_ℓ, a_ℓ), $\ell = 2, 3, 4$, and their ratios. Therefore the spectral decomposition of the symmetric positive definite matrix T is considered in detail and related to the spectral decomposition suggested earlier (Pantleon, 2005; Pantleon *et al.*, 2008; He *et al.*, 2008; Krog-Pedersen *et al.*, 2009).

If T is a (4×4) positive definite symmetric matrix, then the decomposition

$$T = V\Lambda V^{\mathsf{T}} \quad (17)$$

exists where

$$\Lambda = \begin{pmatrix} \lambda_1 & 0 & 0 & 0 \\ 0 & \lambda_2 & 0 & 0 \\ 0 & 0 & \lambda_3 & 0 \\ 0 & 0 & 0 & \lambda_4 \end{pmatrix} \quad (18)$$

is the (4×4) diagonal matrix of eigenvalues $\lambda_1, \ldots, \lambda_4$, and where $V = (a_1, a_2, a_3, a_4)$ is the (4×4) matrix comprising the corresponding column eigenvectors $a_1, \ldots, a_4 \in \mathbb{R}^4$. Equivalently,

$$V^{\mathsf{T}}TV = \Lambda. \quad (19)$$

Here, the matrix T is given in terms of a set of unit vectors $q_1, \ldots, q_n \in \mathbb{S}^3 \subset \mathbb{R}^4$ as

$$T = \frac{1}{n}\sum_{\ell=1}^{n} q_\ell q_\ell^{\mathsf{T}} = \frac{1}{n}\, Q_n Q_n^{\mathsf{T}}, \quad (20)$$

where Q_n is the $(4 \times n)$ matrix composed of column vectors $q_1, \ldots, q_n$. Hence, T is symmetric and positive definite. Let p^* denote the conjugate of an arbitrary quaternion p. Considering the set $q_1 p^*, \ldots, q_n p^* \in \mathbb{S}^3$, *i.e.* the set of disorientations with respect to p, and the corresponding

$$T^* = \frac{1}{n}\sum_{\ell=1}^{n}(q_\ell p^*)(q_\ell p^*)^{\mathsf{T}} = \frac{1}{n}\sum_{\ell=1}^{n}(R_{p^*}q_\ell)(R_{p^*}q_\ell)^{\mathsf{T}} = R_{p^*}\, T\, R_{p^*}^{\mathsf{T}}, \quad (21)$$

the decomposition is

$$\widetilde{V}^{\mathsf{T}} T^* \widetilde{V} = (R_{p^*}V)^{\mathsf{T}}\,(R_{p^*}\, T\, R_{p^*}^{\mathsf{T}})\,(R_{p^*}V) = V^{\mathsf{T}}TV = \Lambda \quad (22)$$

with $\widetilde{V} = R_{p^*}^{\mathsf{T}}V$ composed of column eigenvectors $\widetilde{a}_\ell = a_\ell p^*, \ell = 1, \ldots, 4$, with respect to eigenvalues $\lambda_\ell, \ell = 1, \ldots, 4$. The analogue is true for the multiplication with p^* from the left.

In particular, if $p = a_1$, then $\widetilde{a}_1 = (1, 0, 0, 0)^{\mathsf{T}}$, *i.e.* multiplication with a_1^* from the right acts like centring the measurements at the identity rotation $(1, 0, 0, 0)^{\mathsf{T}}$. In this case $\widetilde{V}$ is of the form

$$\widetilde{V} = \begin{pmatrix} 1 & 0 & 0 & 0 \\ 0 & \widetilde{w}_{11} & \widetilde{w}_{21} & \widetilde{w}_{31} \\ 0 & \widetilde{w}_{12} & \widetilde{w}_{22} & \widetilde{w}_{32} \\ 0 & \widetilde{w}_{13} & \widetilde{w}_{23} & \widetilde{w}_{33} \end{pmatrix} = \begin{pmatrix} 1 & \mathbf{0}^{\mathsf{T}} \\ \mathbf{0} & \widetilde{W} \end{pmatrix} \quad (23)$$

with the (3×3) matrix $\widetilde{W}$ composed of the (3×1) column vectors

$$\widetilde{w}_\ell = a_{\ell+1}a_1^*|_{\mathbb{R}^3}, \qquad \ell = 1, 2, 3, \quad (24)$$

where $a_{\ell+1}a_1^* = \widetilde{a}_{\ell+1}$ are restricted to $\mathbb{R}^3$ by omitting the zero scalar part of the quaternions $\widetilde{a}_{\ell+1}$, $\ell = 1, 2, 3$. Then

$$\widetilde{V}^{\mathsf{T}} = \begin{pmatrix} 1 & \mathbf{0}^{\mathsf{T}} \\ \mathbf{0} & \widetilde{W}^{\mathsf{T}} \end{pmatrix}. \tag{25}$$

Accordingly, T^* may be rewritten explicitly as

$$T^* = \begin{pmatrix} t_{11}^* & t_{12}^* & t_{13}^* & t_{14}^* \\ t_{21}^* & t_{22}^* & t_{23}^* & t_{24}^* \\ t_{31}^* & t_{32}^* & t_{33}^* & t_{34}^* \\ t_{41}^* & t_{42}^* & t_{43}^* & t_{44}^* \end{pmatrix} = \begin{pmatrix} t_{11}^* & t_{12}^* & t_{13}^* & t_{14}^* \\ t_{21}^* & & & \\ t_{31}^* & & \widetilde{T}^* & \\ t_{41}^* & & & \end{pmatrix} \tag{26}$$

with

$$\widetilde{T}^* = \begin{pmatrix} t_{22}^* & t_{23}^* & t_{24}^* \\ t_{32}^* & t_{33}^* & t_{34}^* \\ t_{42}^* & t_{43}^* & t_{44}^* \end{pmatrix}. \tag{27}$$

The (3×3) lower-right submatrix $\widetilde{T}^*$ of T^* corresponds to the matrix Q [equation (13) of Pantleon, 2005].

Eventually

$$\widetilde{V}^{\mathsf{T}} T^* \widetilde{V} = \begin{pmatrix} t_{11}^* & \sum t_{1,j+1}^* \widetilde{w}_{1,j} & \sum t_{1,j+1}^* \widetilde{w}_{2,j} & \sum t_{1,j+1}^* \widetilde{w}_{3,j} \\ \sum t_{i+1,1}^* \widetilde{w}_{1,i} & & & \\ \sum t_{i+1,2}^* \widetilde{w}_{2,i} & & \widetilde{W}^{\mathsf{T}} \widetilde{T}^* \widetilde{W} & \\ \sum t_{i+1,3}^* \widetilde{w}_{3,i} & & & \end{pmatrix} = \Lambda \tag{28}$$

or, equivalently,

$$\widetilde{W}^{\mathsf{T}} \widetilde{T}^* \widetilde{W} = \widetilde{\Lambda} = \begin{pmatrix} \lambda_2 & 0 & 0 \\ 0 & \lambda_3 & 0 \\ 0 & 0 & \lambda_4 \end{pmatrix}. \tag{29}$$

Thus, if a_ℓ, $\ell = 1, \ldots, 4$, are the eigenvectors of T with respect to eigenvalues $\lambda_1, \ldots, \lambda_4$, then $\widetilde{w}_\ell = a_{\ell+1}a_1^*|_{\mathbb{R}^3}$, $\ell = 1, 2, 3$, equation (24), are the eigenvectors of the (3×3) lower-right submatrix $\widetilde{T}^*$ of T^* with respect to eigenvalues $\lambda_2, \lambda_3, \lambda_4$.

4. Inferential statistics

4.1. Inferential statistics with respect to the Bingham quaternion distribution

Neglecting the spatial dependence of EBSD data from individual crystalline grains, the Bingham quaternion distribution

$$f(\pm q; A) = \left[{}_1F_1(1/2; 2; A)\right]^{-1} \exp(q^{\mathsf{T}} A q) \tag{30}$$

with a random $q \in \mathbb{S}^3$, with a symmetric (4×4) matrix A, and with the hypergeometric function ${}_1F_1(1/2; 2; \circ)$ of matrix argument seems appropriate (Bingham, 1964, 1974; Schaeben, 1993; Kunze & Schaeben, 2004, 2005). It is emphasized that the densities $f(\pm q; A)$ and $f(\pm q; A + tI)$, with $t \in \mathbb{R}$ and the (4×4) identity matrix I, define the same distribution. Furthermore, these densities form a transformation model under the group O(4). For $U \in \mathrm{O}(4)$

$$f(\pm Uq; UAU^{\mathsf{T}}) = f(\pm q; A) \tag{31}$$

implying that

$${}_1F_1\left(1/2; 2; UAU^{\mathsf{T}}\right) = {}_1F_1(1/2; 2; A). \tag{32}$$

In particular, if

$$A = U^{\mathsf{T}} K U \tag{33}$$

with U orthonormal and $K = \mathrm{diag}(\kappa_1, \ldots, \kappa_4)$, then

$${}_1F_1(1/2; 2; A) = {}_1F_1(1/2; 2; K) \tag{34}$$

and, therefore, the estimates of the parameters of the Bingham quaternion distribution based on the sample $q_1, \ldots, q_n$ are given by

$$\widehat{U} = V^{\mathsf{T}}, \tag{35}$$

$$\frac{\partial \log {}_1F_1(1/2; 2; K)}{\partial \kappa_i}\Big|_{K=\hat{K}} = \lambda_i, \quad i = 1, \ldots, 4. \tag{36}$$

It should be noted that equation (36) determines $\hat{\kappa}_i$, $i = 1, \ldots, 4$, only up to an additive constant, because $\hat{\kappa}_i$ and $\hat{\kappa}_i + t$, $i = 1, \ldots, 4$, result in the same λ_i, $i = 1, \ldots, 4$. Uniqueness could be conventionally imposed by setting $\hat{\kappa}_4 = 0$.

Provided that $\kappa_1 > \kappa_2, \kappa_3, \kappa_4$ calculation shows that

$$q^{\mathsf{T}} A q = q^{\mathsf{T}} U^{\mathsf{T}} K U q = x^{\mathsf{T}} K x = \kappa_1 - \frac{1}{2} \sum_{j=2}^{4} \frac{x_j^2}{\sigma_j^2}, \tag{37}$$

where $x = (x_1, x_2, x_3, x_4)^{\mathsf{T}} = Uq$ and $\sigma_j^2 = [2(\kappa_1 - \kappa_j)]^{-1}$ for $j = 2, 3, 4$. Thus if q has the Bingham distribution with parameter matrix A and $\kappa_1 - \kappa_j \to \infty$ for $j = 2, 3, 4$, then $\pm x$ tends to $\pm(1, 0, 0, 0)^{\mathsf{T}}$ and the distribution of $(x_2/\sigma_2, x_3/\sigma_3, x_4/\sigma_4)^{\mathsf{T}}$ tends to that of three independent standard normal random variables. Then for $j = 2, 3, 4$, $\lambda_j \simeq E(x_j^2) \simeq \sigma_j^2$, and so

$$\kappa_j - \kappa_1 \simeq -(2\lambda_j)^{-1}. \tag{38}$$

Since we expect that $\kappa_1 - \kappa_j$ and $\hat{\kappa}_1 - \hat{\kappa}_j$, $j = 2, \ldots, 4$, are very large, the interesting statistical issue is to test rotational symmetry, *i.e.* to test the null hypothesis of spherical symmetry that $\kappa_2 = \kappa_3 = \kappa_4$. If this hypothesis can be rejected we would be interested in distinguishing the 'prolate' case, $\kappa_2 > \kappa_3 = \kappa_4$, and the 'oblate' case, $\kappa_2 = \kappa_3 > \kappa_4$.

Assuming rotational symmetry, *i.e.* degeneracy of the Bingham to the Watson distribution, the test statistic

$$T_{\mathrm{s}}^{\mathrm{Bingham}} = n \sum_{\ell=2}^{4} (\widehat{\kappa}_\ell - \overline{\kappa})(\lambda_\ell - \overline{\lambda}) \sim \chi_5^2, \quad n \to \infty, \tag{39}$$

where

$$\overline{\kappa} = \frac{1}{3} \sum_{\ell=2}^{4} \hat{\kappa}_\ell, \quad \overline{\lambda} = \frac{1}{3} \sum_{\ell=2}^{4} \lambda_\ell \tag{40}$$

(Mardia & Jupp, 2000, p. 234). For a given sample of individual orientation measurements $q_1, \ldots, q_n$ we compute the value t_{s} and the corresponding

$$p = \mathrm{Prob}\,(T_{\mathrm{s}} > t_{\mathrm{s}}), \tag{41}$$

and conclude that the null hypothesis of rotational symmetry may be rejected for any significance level $\alpha > p$.

If the hypothesis of spherical symmetry is rejected, we test for prolateness using

$$T_{\mathrm{p}}^{\mathrm{Bingham}} = \frac{n}{2}(\hat{\kappa}_3 - \hat{\kappa}_4)(\lambda_3 - \lambda_4) \sim \chi^2_2, \quad n \to \infty, \tag{42}$$

or, analogously, for oblateness using

$$T_{\mathrm{o}}^{\mathrm{Bingham}} = \frac{n}{2}(\hat{\kappa}_2 - \hat{\kappa}_3)(\lambda_2 - \lambda_3) \sim \chi^2_2, \quad n \to \infty. \tag{43}$$

According to equation (38), for $1 \simeq \lambda_1 \gg \lambda_2 \geq \lambda_3 \geq \lambda_4$ we may apply the asymptotics

$$\kappa_j \simeq \widetilde{\kappa}_j = -(2\lambda_j)^{-1} \quad (j = 2, 3, 4), \tag{44}$$

assuming $\kappa_1 \simeq \widetilde{\kappa}_1 = 0$. Then the test statistics T^{Bingham} simplify to

$$T_{\mathrm{s}}^{\mathrm{Bingham}} \simeq T_{\mathrm{s}}^{\mathrm{asymp\,Bingham}} = \frac{n}{6} \sum_{i=2,3,4} \sum_{j=2,3,4} \left(\frac{\lambda_i}{\lambda_j} - 1 \right), \tag{45}$$

$$T_{\mathrm{p}}^{\mathrm{Bingham}} \simeq T_{\mathrm{p}}^{\mathrm{asymp\,Bingham}} = \frac{n}{4} \left(\frac{\lambda_3}{\lambda_4} + \frac{\lambda_4}{\lambda_3} - 2 \right), \tag{46}$$

$$T_{\mathrm{o}}^{\mathrm{Bingham}} \simeq T_{\mathrm{o}}^{\mathrm{asymp\,Bingham}} = \frac{n}{4} \left(\frac{\lambda_2}{\lambda_3} + \frac{\lambda_3}{\lambda_2} - 2 \right). \tag{47}$$

Note that three summands in equation (45) vanish and that the λ_j are arranged in decreasing order. These formulae agree well with the common-sense interpretation of a spherical, prolate and oblate shape, respectively.

4.2. Inferential statistics without parametric assumptions

Dropping the assumption that $\pm q$ has a Bingham distribution and applying large-sample approximation the tedious numerics with respect to ${}_1F_1$ can be avoided; only

$$c_{ij} = \frac{1}{n} \sum_{\ell=1}^{n} (q_\ell^{\mathsf{T}} a_i)^2 (q_\ell^{\mathsf{T}} a_j)^2 \tag{48}$$

is required, where $a_i, i = 1, \ldots, 4$, are the eigenvectors of T corresponding to the eigenvalues $\lambda_1 \geq \lambda_2 \geq \lambda_3 \geq \lambda_4$. Analogously to results (Prentice, 1984, §6, 1986, §5; Mardia & Jupp, 2000, §10.7.2) the test statistics are, for the spherical case,

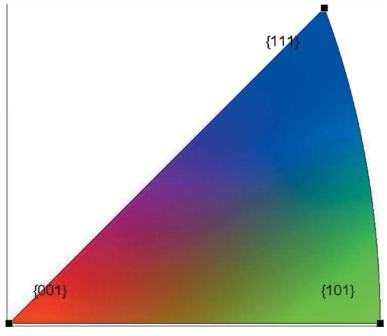

Figure 1
Inverse pole figure colour bar.

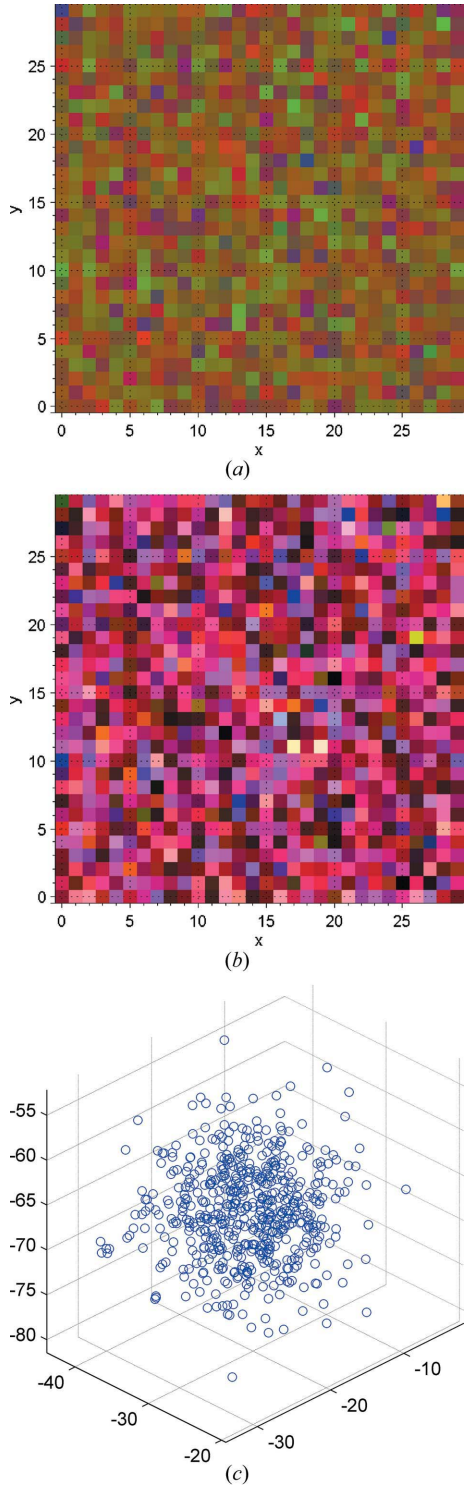

Figure 2
900 simulated spatially indexed individual orientations from the Bingham quaternion distribution with modal orientation $q_{\mathrm{modal}} =$ (0.78124, 0.26042, 0.15035, 0.54703) and dispersion parameters $K =$ diag (340, 0, 0, 0) in a 30×30 grid as a colour-coded orientation map according to the (100) inverse pole figure colour bar (*a*) and RGB colours (*b*) and as a three-dimensional axis–angle scatter plot centred at the mean orientation (*c*).

$$T_s = 15n\frac{\lambda_2^2+\lambda_3^2+\lambda_4^2-(1-\lambda_1)^2/3}{2(1-2\lambda_1+c_{11})} \sim \chi_5^2, \quad n\to\infty, \quad (49)$$

for the prolate case,

$$T_p = 8n\frac{\lambda_3^2+\lambda_4^2-(1-\lambda_1-\lambda_2)^2/2}{2[1-2(\lambda_1+\lambda_2)+c_{11}+2c_{12}+c_{22}]} \sim \chi_2^2, \quad n\to\infty, \quad (50)$$

and for the oblate case,

$$T_o = 8n\frac{\lambda_2^2+\lambda_3^2-(1-\lambda_1-\lambda_4)^2/2}{2[1-2(\lambda_1+\lambda_4)+c_{11}+2c_{14}+c_{44}]} \sim \chi_2^2, \quad n\to\infty. \quad (51)$$

For details concerning inferential statistics the reader is referred to Appendix *A*. Some details of the computation and asymptotics are given in Appendix *B*.

5. Practical applications

Several samples of individual orientation measurements are analysed. The first sample, referred to as simIOM, is a set of simulated measurements; the following three samples are actual measurements on oxygen-free high-conductivity copper, deformed to 25% in tension (Krog-Pedersen *et al.*, 2009).

The data are displayed as follows:

(*a*) Orientation maps applying the colour coding given by the inverse pole figure colour bar as shown in Fig. 1 to the specimen *x* direction, and

(*b*) applying RGB colour coding of Euler angles $(\varphi_1, \phi, \varphi_2)$ according to Bunge's *zxz* convention, where the Euler angle φ_1 is associated with red, ϕ with green and φ_2 with blue. For the simulated EBSD data, the units along both axes of the orientation map are just pixels; for the experimental data, the unit is 1 µm for both axes of the orientation map. Thus each pixel of the map corresponds to one experimental orientation. The labels along the axes refer to the origin of the coordinate

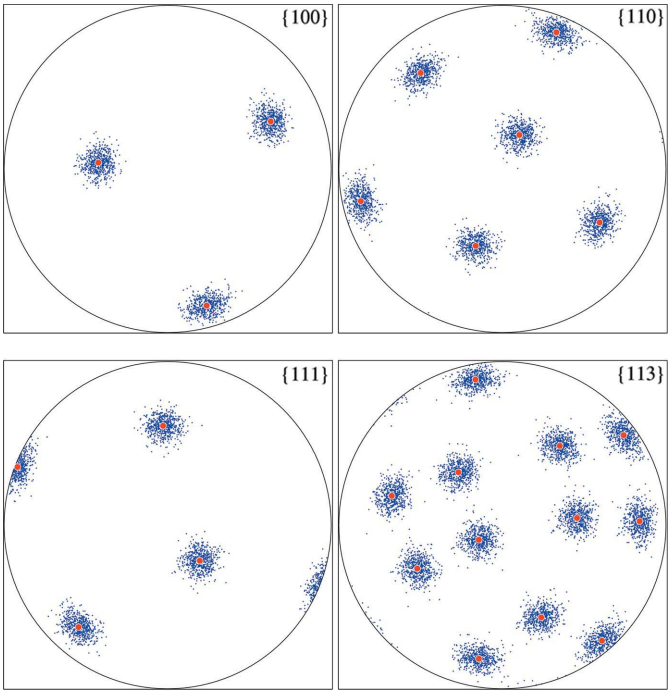

Figure 3
Pole point plots for crystallographic forms {100}, {110}, {111} and {113} of 900 simulated spatially indexed individual orientations from the Bingham quaternion distribution, augmented with the mean orientation marked by a red dot emphasizing a small dispersion.

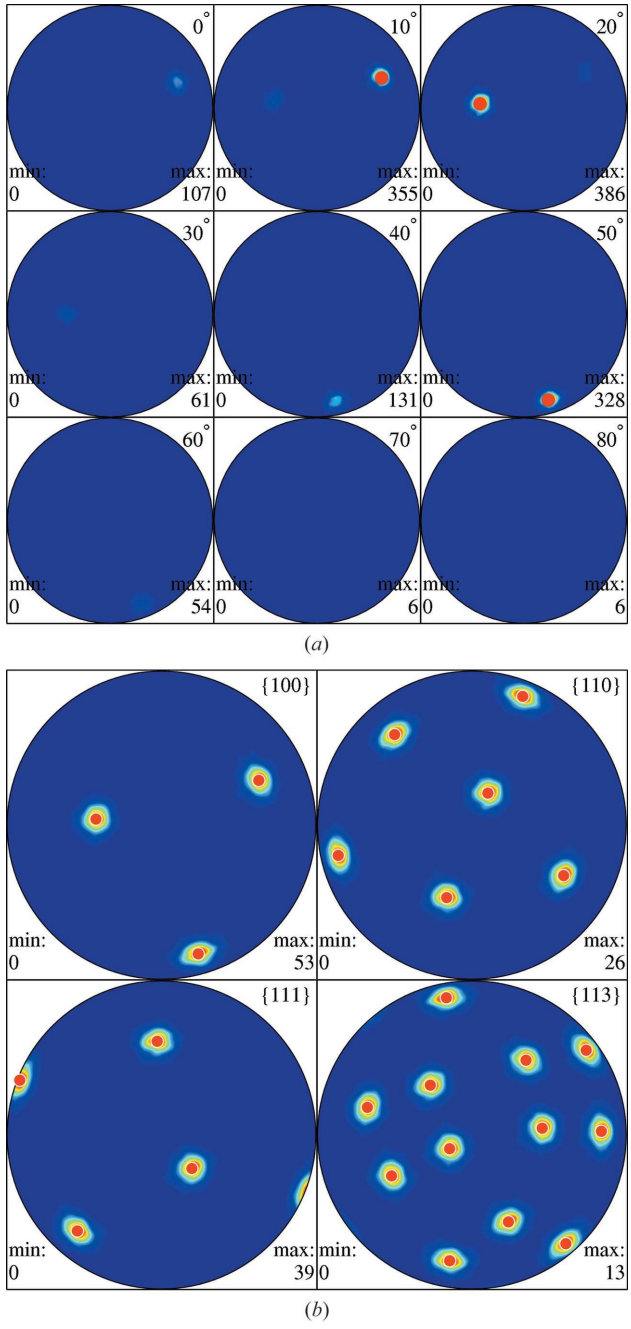

Figure 4
σ-Sections of orientation density function (*a*) and pole density functions for crystallographic forms {100}, {110}, {111} and {113} (*b*) of 900 simulated spatially indexed individual orientations according to the Bingham quaternion distribution, augmented with the mean orientation marked by a red dot.

system attached to the specimen comprising not just the analysed grain.

(*c*) A three-dimensional scatter plot with respect to axis–angle parametrization, *i.e.* $\omega\mathbf{n} = \omega(n_x, n_y, n_z)^{\mathsf{T}}$ with $\omega \in [0, 180]$ and $\mathbf{n} \in \mathbb{S}^2$ are displayed in a Cartesian (x, y, z)-coordinate system. No provision whatsoever is made for the spherical metric of the axis–angle parametrization.

(*d*) Pole points $q_\ell \tilde{G}_{\text{Laue}} h \tilde{G}^*_{\text{Laue}} q^*_\ell$, $\ell = 1, \ldots, n$, for some crystallographic forms $h \in \mathbb{S}^2$, *i.e.* crystallographic directions and their symmetrical equivalents $\tilde{G}_{\text{Laue}} h \tilde{G}^*_{\text{Laue}}$, and

(*e*) plots of the orientation density and

(*f*) pole density function.

Here, orientation maps are used for a rough indication of spatial dependence only.

The orientation density function is computed by non-parametric kernel density estimation with the de la Vallée Poussin kernel, and corresponding pole density functions are determined as superpositions of the totally geodesic Radon transform of the de la Vallée Poussin kernel.

In all cases the orientation tensor T and its eigenvalues and eigenvectors are computed, and the shape parameters are derived such that the smallest estimated shape parameter eventually equals 0 whatever formula was used for its computation. Since the Bingham test statistics involve differences of estimated shape parameters they are independent of the way the shape parameters are determined as the differently estimated shape parameters differ by additive terms only. Then the spherical, oblate and prolate cases are tested, if reasonable.

All computations have been done with our free and open-source *Matlab* toolbox *MTEX 3.0*, which can be downloaded from http://code.google.com/p/mtex/.

5.1. Simulated EBSD data

The first data set was fabricated by simulation of 900 (pseudo-)independent spatially indexed individual orientation measurements from a given Bingham quaternion distribution with modal orientation $q_{\text{modal}} = (0.78124, 0.26042, 0.15035, 0.54703)$ [$(65°, 35°, 5°)$ in Euler angles according to Bunge's zxz convention] and dispersion parameters $K = \text{diag}(340, 0, 0, 0)$ in a 30×30 grid. Assuming cubic crystal symmetry the 900 simulated orientation data are displayed as orientation maps of 30×30 pixels and as a three-dimensional scatter plot with respect to axis–angle parametrization in Fig. 2, as pole point plots of crystallographic forms $\tilde{G}_{\text{Laue}} h$ (100), (110), (111) and (113) in Fig. 3, and as pole and orientation densities in Fig. 4.

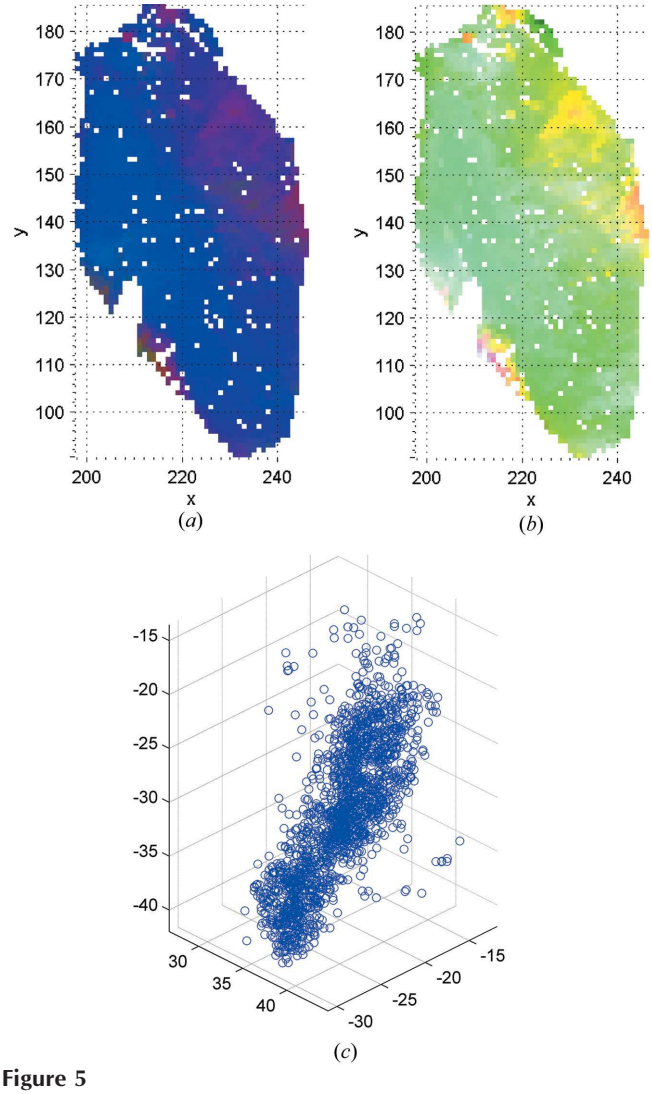

Figure 5
Grain 40 with 3068 spatially indexed individual orientations as a colour-coded orientation map according to the (100) inverse pole figure colour bar (*a*) and RGB colours (*b*) and as a three-dimensional axis–angle scatter plot centred at the mean orientation (*c*).

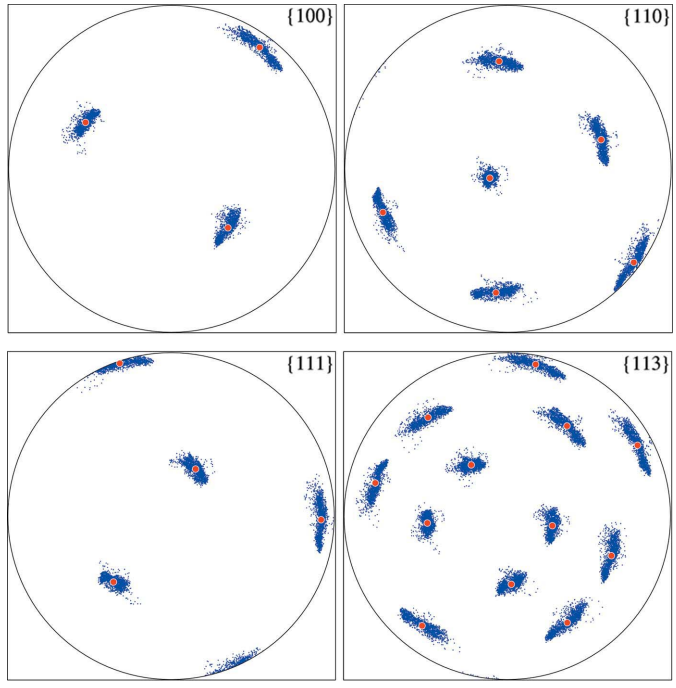

Figure 6
Pole point plots of grain 40 for crystallographic forms {100}, {110}, {111} and {113}, augmented with the mean orientation marked by a red dot emphasizing a small dispersion.

For these simulated data the estimated texture index $I = 61.2971$ and entropy $E = -3.6491$. The eigenvalues are for $i = 1, \ldots, 4$, $\lambda_i = 0.9954, 0.0016, 0.0015, 0.0014$, respectively, and their ratios are $\lambda_2/\lambda_3 = 1.1043$, $\lambda_3/\lambda_4 = 1.0517$.

5.2. Experimental EBSD data

Experimental orientation data were collected on a deformed oxygen-free high-conductivity copper with a purity of 99.99%. The starting material was recrystallized to a grain size (mean linear intercept length excluding twin boundaries obtained by EBSD) of about 30 µm. A cylindrical dog-bone ASTM standard tensile specimen with a gauge area of ø4 × 20 mm was prepared by spark-cutting and loaded in tension on an INSTRON testing machine with a cross-head speed of 0.5 mm min^{-1} till failure. The ultimate tensile strength was reached at 25% strain. Part of the gauge section of the deformed specimen was cut out and half the sample was ground away so that the longitudinal midsection was exposed. After further polishing, the sample was finally electro-polished in preparation for the EBSD investigation. Using a scanning electron microscope (Zeiss SUPRA 35) equipped with a field emission gun and a Nordlys2 detector, lattice orientations on a central section of the specimen (comprising the tensile direction) were recorded with the *Channel5* software from HKL Technology (Hobro, Denmark). The investigated regions are well outside the neck and only the homogeneously deformed part is analysed (Krog-Pedersen *et al.*, 2009).

Orientations were determined on the longitudinal midsection in a square grid of 1100 × 800 points with a distance of 1 µm between measuring points. The disorientations between

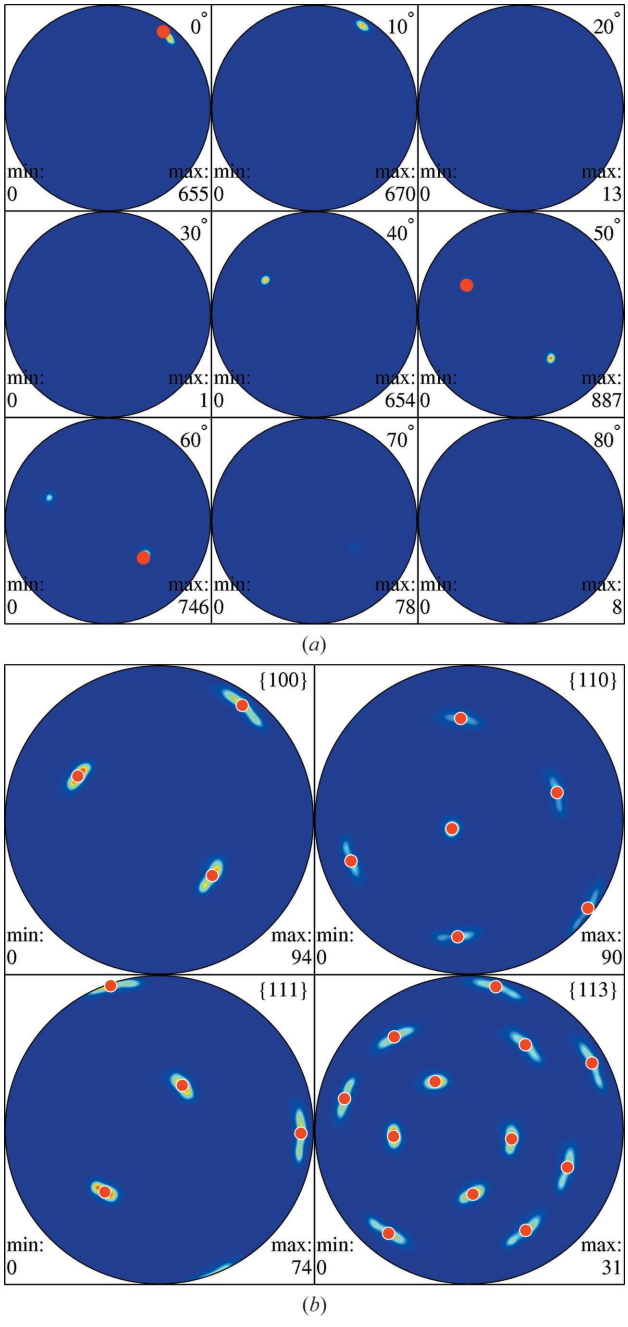

Figure 7
σ-Sections of orientation density function (*a*) and pole density functions for crystallographic forms {100}, {110}, {111} and {113} (*b*) of spatially indexed individual orientations of grain 40, augmented with the mean orientation marked by a red dot.

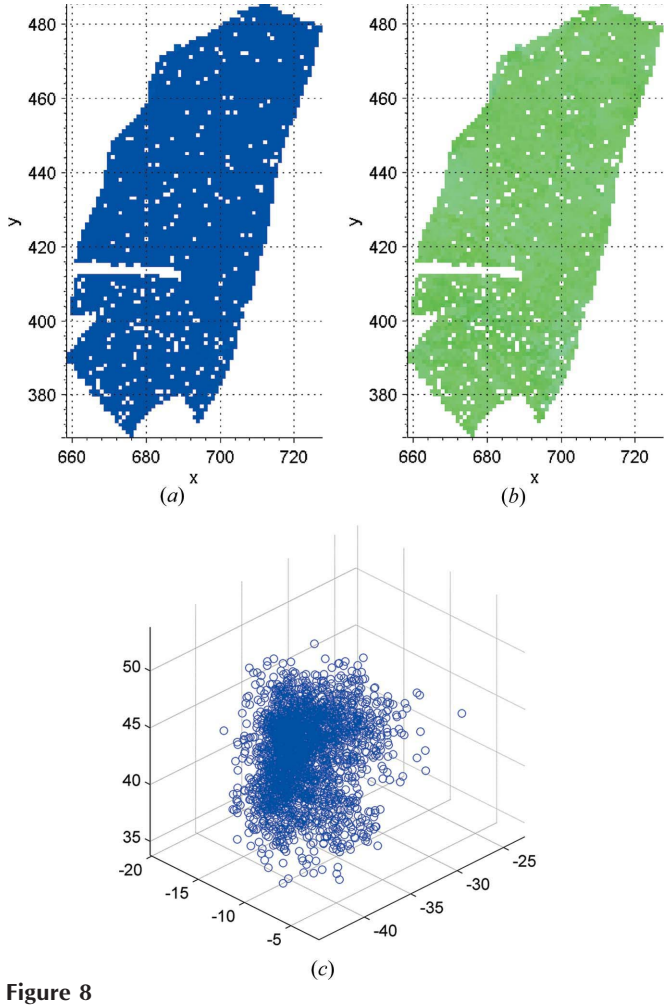

Figure 8
Grain 147 with 4324 spatially indexed individual orientations as a colour-coded orientation map according to the (100) inverse pole figure colour bar (*a*) and RGB colours (*b*) and as a three-dimensional axis–angle scatter plot centred at the mean orientation (*c*).

all neighbouring points were calculated taking into account the cubic symmetry of the face-centred cubic crystalline lattice of copper. Grains are identified as contiguous areas fully surrounded by boundaries with disorientation angles larger than 7° separating them from neighbouring grains. Three large grains were selected to represent different shapes of orientation distributions; their orientation maps are presented in Figs. 5, 8 and 11, with the tensile axis displayed vertically. Owing to the medium stacking-fault energy of copper, many twins are present which can be recognized in the orientation maps as twin lamellae (*e.g.* the horizontal white cut in the grain shown in Fig. 8).

Next we shall analyse the distribution of crystallographic orientations of three individual grains, labelled grain 40, grain 147 and grain 109.

The data of grain 40 are depicted as colour-coded orientation maps and as a three-dimensional axis–angle scatter plot centred at the identity in Fig. 5, as pole point plots in Fig. 6, and as pole density and orientation densities in Fig. 7.

In the same way, the data of grain 147 are depicted in Figs. 8, 9 and 10. Figs. 11, 12 and 13 display the data of grain 109.

The analyses of the orientation data, in particular the spectral analyses of the orientation matrices T, are summarized numerically in Tables 1 and 2.

The orientation maps of grain 40 (Fig. 5) exhibit only gentle colour variations, corresponding to a unimodal orientation density function (Fig. 7). Its pole point plots (Fig. 6) reveal best that the distribution is not spherically symmetric with respect to its mean. Only the pole point mode in the centre of the (110) pole point plot is almost spherical, indicating that this is the direction of the axis of internal rotation or bending within the grain, which is confirmed by the vector components of the eigenvector $\mathrm{Vec}(\pm a_2) = \pm(0.0499455, 0.545993, 0.8363)^{\mathsf{T}}$ corresponding to the second largest eigenvalue.

The orientation maps of grain 147 (Fig. 8) are almost uniformly colour coded; all plots seem to indicate spherical symmetry with respect to the unique mode of the orientation density function.

The orientation maps of grain 109 (Fig. 11) indicate that it comprises two parts with distinct orientations, clearly visible as

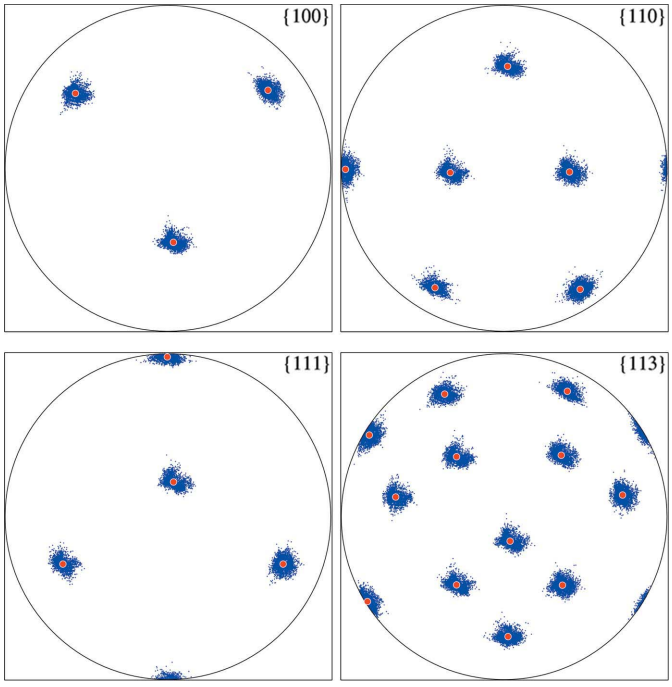

Figure 9
Pole point plots of grain 147 for crystallographic forms {100}, {110}, {111} and {113}, augmented with the mean orientation marked by a red dot emphasizing a small dispersion.

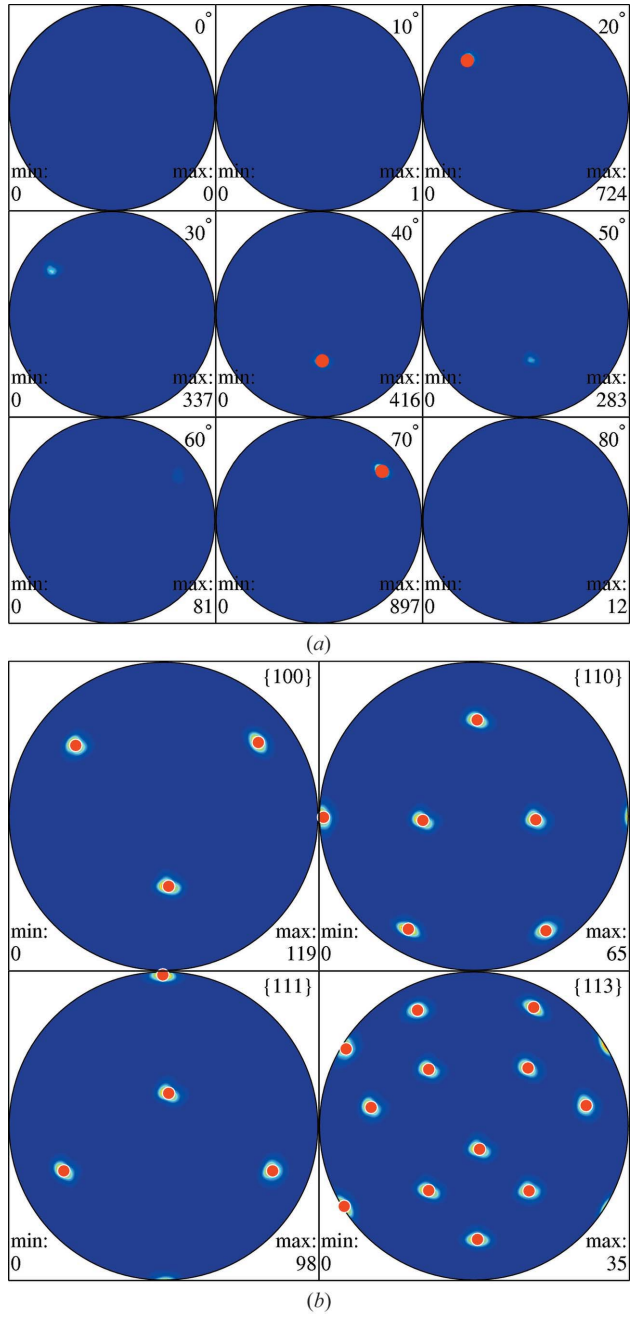

Figure 10
σ-Sections of orientation density function (*a*) and pole density functions for crystallographic forms {100}, {110}, {111} and {113} (*b*) of spatially indexed individual orientations of grain 147, augmented with the mean orientation marked by a red dot.

bimodality in the pole point, pole and orientation density plots (Fig. 13). The centred scatter plots agree roughly with the analyses of the ratios of eigenvalues and the statistical tests.

These differences in the symmetry of the orientation density function originate from the peculiarities of plastic deformation. Crystal plasticity is achieved by glide on crystallographic glide systems: $\{111\}\langle 1\bar{1}0\rangle$ glide systems in the case of copper. Depending on the number of activated glide systems, intragrain disorientations develop with different degrees of freedom for the main rotation axis. For instance, a prolate distribution with a single dominating rotation axis indicates a single degree of freedom in selecting slip systems, whereas spherical symmetric distributions require three degrees of freedom in selecting slip systems (Krog-Pedersen *et al.*, 2009).

6. Conclusions

Conclusions are restricted to rather methodological aspects.

The proper statistic of individual orientation measurements is the orientation tensor T, if independence is assumed. For

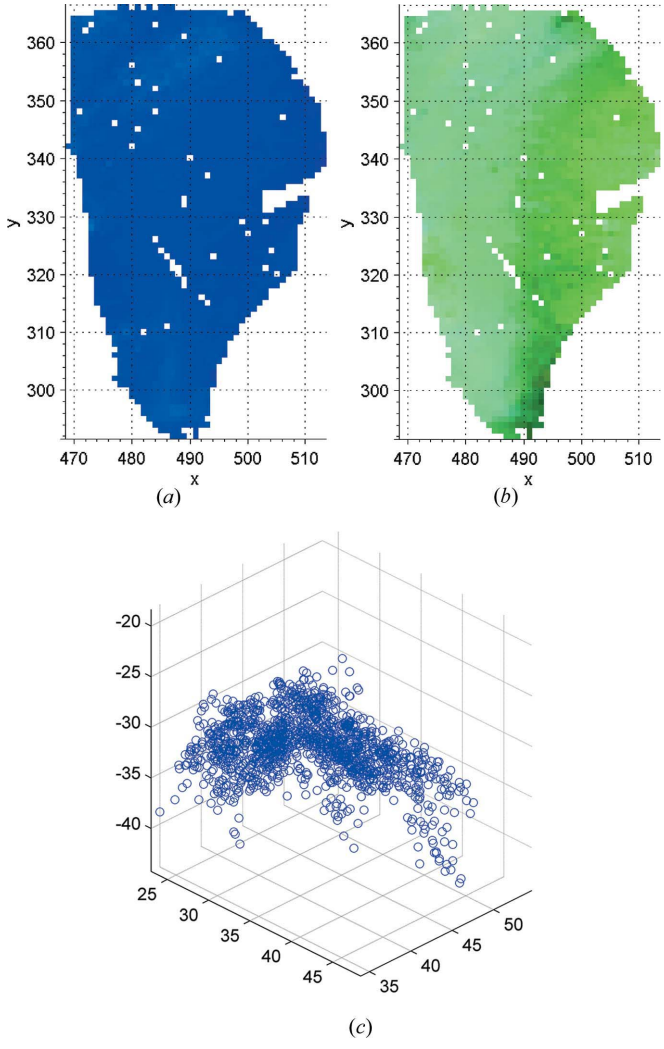

Figure 11
Grain 109 with 2253 spatially indexed individual orientations as a colour-coded orientation map according to the (100) inverse pole figure colour bar (*a*) and RGB colours (*b*) and as a three-dimensional axis–angle scatter plot centred at the mean orientation (*c*).

Table 1
Summary of the spectral analysis of the orientation tensor T for grain 40, grain 147 and grain 109.

Data comprise texture index, entropy, largest eigenvalue λ_1 corresponding to principal axes a_1 of smallest inertia, remaining eigenvalues λ_i and their ratios, and estimated shape parameters κ_i of the Bingham quaternion distribution, involving either equation (36) or the large-concentration approximation, equation (44).

	simIOM	Grain 40	Grain 147	Grain 109
Sample size	900	3068	4324	2253
Texture index	61.2971	337.7395	308.9108	178.4238
Entropy	−3.6491	−5.3425	−5.1136	−4.7782
λ_1	0.9954	0.9965	0.9983	0.9956
λ_2	1.645×10^{-3}	2.928×10^{-3}	8.713×10^{-4}	2.166×10^{-3}
λ_3	1.489×10^{-3}	3.000×10^{-4}	4.989×10^{-4}	1.906×10^{-3}
λ_4	1.416×10^{-3}	2.645×10^{-4}	3.513×10^{-4}	3.120×10^{-4}
λ_2/λ_3	1.1043	9.7599	1.7465	1.1364
λ_3/λ_4	1.0517	1.1345	1.4199	6.1100
Visual inspection	'Spherical'	'Prolate'	'Spherical'	'Oblate'
Computation involving ${}_1F_1$, equation (36)				
κ_1	3.5344×10^2	1.8908×10^3	1.4234×10^3	1.6029×10^3
κ_2	49.037	1.7195×10^3	8.4916×10^2	1.3716×10^3
κ_3	17.354	2.2410×10^2	4.2083×10^2	1.3401×10^3
κ_4	0.0	0.0	0.0	0.0
$\kappa_2 - \kappa_3$	31.6829	1.4954×10^3	4.2832×10^2	31.4763
$\kappa_3 - \kappa_4$	17.3542	2.2410×10^2	4.2083×10^2	1.3401×10^3
Computation applying large-concentration approximation, equation (44)				
κ_1	3.5293×10^2	1.8903×10^3	1.4229×10^3	1.6024×10^3
κ_2	49.037	1.7196×10^3	8.4916×10^2	1.3716×10^3
κ_3	17.354	2.2410×10^2	4.2083×10^2	1.3401×10^3
κ_4	0.0	0.0	0.0	0.0
$\kappa_2 - \kappa_3$	31.6830	1.4956×10^3	4.2832×10^2	31.4763
$\kappa_3 - \kappa_4$	17.3542	2.2410×10^2	4.2083×10^2	1.3401×10^3

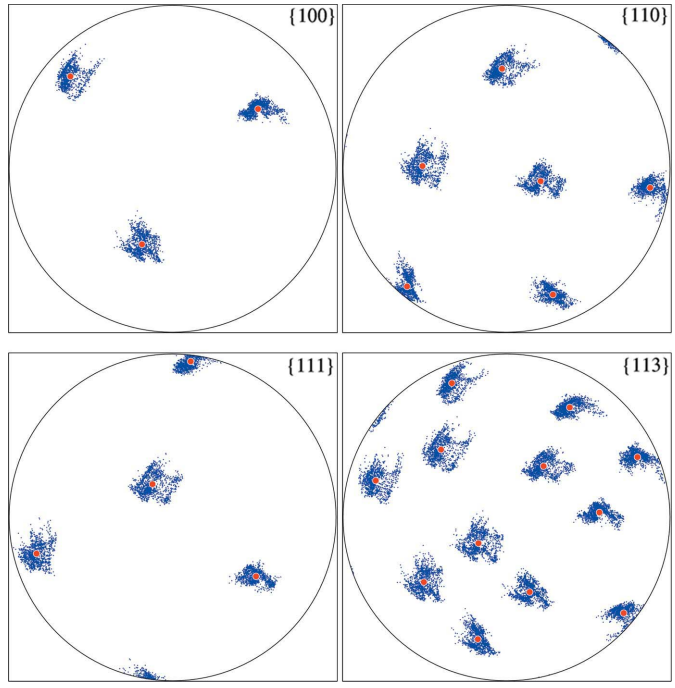

Figure 12
Pole point plots of grain 109 for crystallographic forms {100}, {110}, {111} and {113}, augmented with the mean orientation marked by a red dot emphasizing a small dispersion.

Table 2
Summary of the spectral analysis of the orientation tensor T for grain 40, grain 147 and grain 109.

Data comprise tests for the spherical, oblate and prolate Bingham case applying shape parameters estimated with either equation (36) or the large-concentration approximation, equations (45), (47), (46), respectively, and large-sample approximation tests for spherical, oblate and prolate symmetry, respectively, without parametric assumptions, equations (49), (51), (50). 'a' indicates that the test does not apply, 'no rejection' indicates that rejection at any reasonable level of significance is not possible.

	simIOM	Grain 40	Grain 147	Grain 109
Sample size	900	3068	4324	2253
Bingham statistics involving ${}_1F_1$, equations (39), (42), (43)				
$p_{\text{spherical}}$	0.3895	0	0	0
Spherical	'No rejection'	Reject	Reject	Reject
p_{oblate}		0	0	0.0099
Oblate		Reject	Reject	Reject for $\alpha > p$
p_{prolate}		0.0022	0	0
Prolate		Reject for $\alpha > p$	Reject	Reject
Bingham statistics involving large-concentration approximation, equations (45), (46), (47)				
$p_{\text{spherical}}$	0.3895	0	0	0
Spherical	'No rejection'	Reject	Reject	Reject
p_{oblate}		0	0	0.0100
Oblate		Reject	Reject	Reject for $\alpha > p$
p_{prolate}		0.0022	0	0
Prolate		Reject for $\alpha > p$	Reject	Reject
Large-sample approximation statistics without parametric assumptions, equations (49), (50), (51)				
$p_{\text{spherical}}$	0.4031	0	0	0
Spherical	'No rejection'	Reject	Reject	Reject
p_{oblate}		0	0	0.0043
Oblate		Reject	Reject	Reject for $\alpha > p$
p_{prolate}		0.0418	0	0
Prolate		Reject for $\alpha > p$	Reject	Reject

sufficiently concentrated distributions the first principal axis of inertia (corresponding to the largest eigenvalue of T, *i.e.* the smallest principal moment of inertia) is fairly well approximated by the normalized mean quaternion (and its negative), if special provisions are taken, or by the modal quaternion (and its negative) of some kernel-estimated orientation density. However, neither the normalized mean quaternion nor the modal quaternion leads to inferential statistics.

The ratios of the three remaining small eigenvalues may indicate the geometric shape of the sample of individual orientations. Special cases are oblateness, prolateness or a spherical shape. They may reveal details of the texture-generating processes, as different deformation regimes or differently activated sets of slip systems. While a prolate shape of the distribution may be identified by means of pole point, pole or orientation density plots, oblate and spherical shapes can hardly be distinguished. Three-dimensional scatter plots may give a first hint, but are usually distorted and therefore hard to read.

The ratios of the three small eigenvalues of the orientation tensor T may be interpreted as describing a tendency towards one of the three symmetric cases, if we exclude some special cases by visual inspection of all available plots. From descriptive statistics one proceeds to inferential statistics either applying parametric assumptions with reference to the Bingham quaternion distribution on $\mathbb{S}^3$ or using large-sample approximations avoiding any parametric assumptions. Then significance tests prove the absence of symmetry if they lead to the rejection of the null hypothesis with respect to a given significance.

Comparing the (x, y) plots of the fabricated and the experimental data suggests that one should proceed to methods of spatial statistics as introduced by van den Boogaart & Schaeben (2002*a*,*b*), *e.g.* to capture the spatially induced correlation.

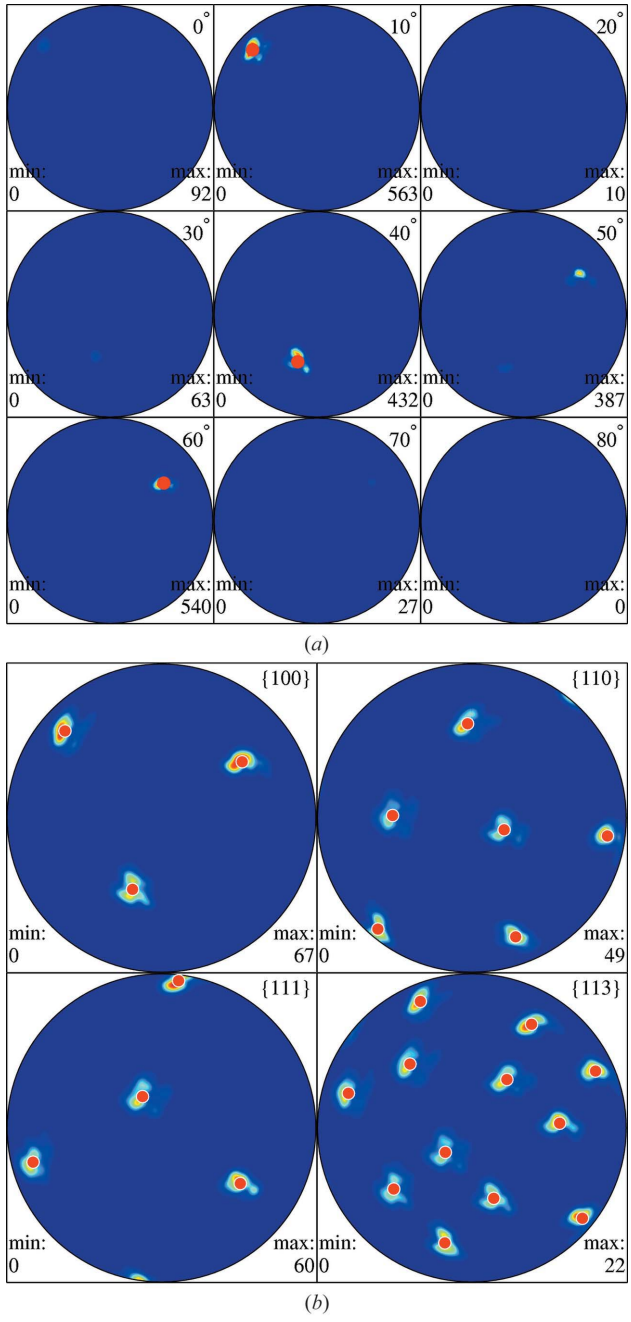

Figure 13
σ-Sections of orientation density function (*a*) and pole density functions for crystallographic forms {100}, {110}, {111} and {113} (*b*) of spatially indexed individual orientations of grain 109, augmented with the mean orientation marked by a red dot.

APPENDIX A
Tests of rotational symmetry of axial distributions

A1. A useful proposition

Proposition. If $X = (X_1, \ldots, X_p)^\mathsf{T}$ is a random vector with

$$X \sim N(0, \alpha I_p - \beta \mathbf{1}\mathbf{1}^\mathsf{T}) \tag{52}$$

then

$$\alpha^{-1} \sum_{i=1}^{p} (X_i - \overline{X})^2 \sim \chi^2_{p-1}. \tag{53}$$

Proof. First note that

$$\begin{aligned} \mathrm{var}(X - \overline{X}\mathbf{1}) &= (I_p - p^{-1}\mathbf{1}\mathbf{1}^\mathsf{T})(\alpha I_p - \beta \mathbf{1}\mathbf{1}^\mathsf{T})(I_p - p^{-1}\mathbf{1}\mathbf{1}^\mathsf{T}) \\ &= \alpha(I_p - p^{-1}\mathbf{1}\mathbf{1}^\mathsf{T}). \end{aligned} \tag{54}$$

Take V independent of X with $V \sim N(0, \alpha/p)$. Then

$$X - \overline{X}\mathbf{1} + V\mathbf{1} \sim N(0, \alpha I_p), \tag{55}$$

and so

$$\alpha^{-1} \sum_{i=1}^{p} (X_i - \overline{X} + V)^2 = \alpha^{-1} \sum_{i=1}^{p} (X_i - \overline{X})^2 + \frac{p}{\alpha} p V^2 \sim \chi^2_p, \tag{56}$$

from which the result follows by Cochran's theorem.

A2. Testing O(p − 2) symmetry of Bingham distributions

Consider the Bingham distributions on $\mathbb{R}P^{p-1}$ with densities

$$f(\pm x; A) = {}_1F_1(1/2; p/2; A)^{-1} \exp(x^\mathsf{T} A x), \tag{57}$$

where $x = (x_1, \ldots, x_p)^\mathsf{T}$ is a random unit vector and A is a symmetric $p \times p$ matrix. We shall use the spectral decomposition

$$A = \sum_{i=1}^{p} \kappa_i \mu_i \mu_i^\mathsf{T} \tag{58}$$

of A, where $\mu_1, \ldots, \mu_p$ are orthonormal vectors and $\kappa_1 \geq \cdots \geq \kappa_p$. We are interested in the hypothesis

$$H_{\mathrm{prolate}} : \kappa_3 = \cdots = \kappa_p \tag{59}$$

of O($p-2$) symmetry of the distribution about the plane spanned by μ_1 and μ_2, and in the hypothesis

$$H_{\mathrm{oblate}} : \kappa_2 = \cdots = \kappa_{p-1} \tag{60}$$

of O($p-2$) symmetry of the distribution about the plane spanned by μ_1 and μ_p.

Observations $\pm x_1, \ldots, \pm x_n$ on $\mathbb{R}P^{p-1}$ can be summarized by the scatter matrix $\overline{T}$ about the origin, defined (see §9.2.10 of Mardia & Jupp, 2000) by

$$\overline{T} = \frac{1}{n} \sum_{i=1}^{n} x_i x_i^\mathsf{T}. \tag{61}$$

Let $\bar{t}_1, \ldots, \bar{t}_p$ (with $\bar{t}_1 \geq \cdots \geq \bar{t}_p$) denote the eigenvalues of $\overline{T}$. From §10.3.37 of Mardia & Jupp (2000), the maximum likelihood estimates $\hat{\kappa}_1, \ldots, \hat{\kappa}_p$ of $\kappa_1, \ldots, \kappa_p$ under the full Bingham model are given by

$$\left. \frac{\partial \log {}_1F_1(1/2; p/2; K)}{\partial \kappa_i} \right|_{K=\hat{K}} = \bar{t}_i, \qquad i = 1, \ldots, p, \tag{62}$$

where $\hat{K} = \mathrm{diag}(\hat{\kappa}_1, \ldots, \hat{\kappa}_p)$. (Recall that $\hat{\kappa}_1, \ldots, \hat{\kappa}_p$ can be determined only up to addition of a constant, since, for any real constant c, the matrices A and $A + cI_p$ give the same distribution.) The maximum likelihood estimates $\tilde{\kappa}_1, \tilde{\kappa}_2, \tilde{\kappa}, \ldots, \tilde{\kappa}$ of $\kappa_1, \ldots, \kappa_p$ under H_{prolate} are given (up to addition of a constant) by

$$\left. \frac{\partial \log {}_1F_1(1/2; p/2; K)}{\partial \kappa_i} \right|_{K=\tilde{K}} = \bar{t}_i, \qquad i = 1, 2, \tag{63}$$

$$\left. \frac{\partial \log {}_1F_1(1/2\ semip/2; K)}{\partial \kappa_3} \right|_{K=\tilde{K}} = \tilde{t}, \tag{64}$$

where $\tilde{K} = \mathrm{diag}(\tilde{\kappa}_1, \tilde{\kappa}_2, \tilde{\kappa}, \ldots, \tilde{\kappa})$ and

$$\tilde{t} = \frac{1}{p-2} \sum_{i=3}^{p} \bar{t}_i. \tag{65}$$

Similarly, the maximum likelihood estimates $\check{\kappa}_1, \check{\kappa}, \ldots, \check{\kappa}, \check{\kappa}_p$ of $\kappa_1, \ldots, \kappa_p$ under H_{oblate} are given (up to addition of a constant) by

$$\left. \frac{\partial \log {}_1F_1(1/2; p/2; K)}{\partial \kappa_i} \right|_{K=\check{K}} = \bar{t}_i, \qquad i = 1, p, \tag{66}$$

$$\left. \frac{\partial \log {}_1F_1(1/2; p/2; K)}{\partial \kappa_2} \right|_{K=\check{K}} = \check{t}, \tag{67}$$

where $\check{K} = \mathrm{diag}(\check{\kappa}_1, \check{\kappa}, \ldots, \check{\kappa}, \check{\kappa}_p)$ and

$$\check{t} = \frac{1}{p-2} \sum_{i=2}^{p-1} \bar{t}_i. \tag{68}$$

It follows from standard results on regular exponential models that the likelihood ratio statistics w_{prolate} and w_{oblate} of H_{prolate} and H_{oblate} satisfy the large-sample approximations

$$w_{\mathrm{prolate}} \simeq \tilde{w}_{\mathrm{prolate}} = n \sum_{i=3}^{p} (\hat{\kappa}_i - \tilde{\kappa})(\bar{t}_i - \tilde{t}), \tag{69}$$

$$w_{\mathrm{oblate}} \simeq \check{w}_{\mathrm{oblate}} = n \sum_{i=2}^{p-1} (\hat{\kappa}_i - \check{\kappa})(\bar{t}_i - \check{t}). \tag{70}$$

In the case $p = 4$, equations (69) and (70) can be rewritten as

$$w_{\mathrm{prolate}} \simeq \tilde{w}_{\mathrm{prolate}} = \frac{n}{2} (\hat{\kappa}_3 - \hat{\kappa}_4)(\bar{t}_3 - \bar{t}_4), \tag{71}$$

$$w_{\mathrm{oblate}} \simeq \check{w}_{\mathrm{oblate}} = \frac{n}{2} (\hat{\kappa}_2 - \hat{\kappa}_3)(\bar{t}_2 - \bar{t}_3). \tag{72}$$

The parameter matrix A of a Bingham distribution in H_{prolate} is specified by the pair of orthogonal p vectors $\kappa_1 \mu_1$ and $\kappa_2 \mu_2$,

and so the dimension of $H_{\rm prolate}$ is $p+(p-1)$. Similarly, the parameter matrix A of a Bingham distribution in $H_{\rm oblate}$ is specified by the pair of orthogonal p vectors $\kappa_1\mu_1$ and $\kappa_p\mu_p$, and so the dimension of $H_{\rm oblate}$ is $p+(p-1)$. The parameter space of the Bingham distributions has dimension $p(p+1)/2-1$. Thus the codimension of both $H_{\rm prolate}$ and $H_{\rm oblate}$ is

$$[p(p+1)/2-1]-[p+(p-1)]=\frac{p(p-3)}{2}. \tag{73}$$

It follows from standard results on likelihood ratio statistics that the (large-sample) asymptotic distributions of $\tilde{w}_{\rm prolate}$ and $\check{w}_{\rm oblate}$ (and $w_{\rm prolate}$ and $w_{\rm oblate}$) under the null hypotheses $H_{\rm prolate}$ and $H_{\rm oblate}$ are

$$\tilde{w}_{\rm prolate} \,\tilde{\sim}\, \chi^2_{p(p-3)/2}, \tag{74}$$

$$\check{w}_{\rm oblate} \,\tilde{\sim}\, \chi^2_{p(p-3)/2}, \tag{75}$$

where $\,\tilde{\sim}\,$ means 'is asymptotically distributed as' (provided that $\kappa_1>\kappa_2>\kappa_3$ in the prolate case and $\kappa_1>\kappa_2$ and $\kappa_{p-1}>\kappa_p$ in the oblate case).

A3. A large-sample test of SO($p-r$) symmetry

In this section we drop the assumption that $\pm x$ has a Bingham distribution. We are interested in the hypothesis of O($p-r$) symmetry of the distribution about the r-dimensional subspace spanned by r orthonormal vectors $\mu_1,\ldots,\mu_r$. Without loss of generality, we can take the unit eigenvectors of $E(xx^{\rm T})$ to be $\mu_1,\ldots,\mu_p$ with $\mu_i=(\underbrace{0,\ldots,0}_{i-1},1,0,\ldots,0)$ for $i=1,\ldots,p$. Put

$$c_{ij}=E(x_i^2x_j^2), \qquad 1\le i,j\le p. \tag{76}$$

Under O($p-r$) symmetry, the matrices $[E(x_ix_j)]$ and (c_{ij}) have the form

$$[E(x_ix_j)]=\begin{bmatrix}\mathrm{diag}(\lambda_1,\ldots,\lambda_r) & \mathbf{0}\\ \mathbf{0} & \lambda I_{p-r}\end{bmatrix} \tag{77}$$

and

$$(c_{ij})=\begin{pmatrix} c_{11} & \ldots & c_{1r} & c_{1,r+1}\mathbf{1}^{\rm T}\\ c_{21} & \ldots & c_{2r} & c_{2,r+1}\mathbf{1}^{\rm T}\\ \vdots & \ddots & \ddots & \vdots\\ c_{r1} & \ldots & c_{rr} & c_{r,r+1}\mathbf{1}^{\rm T}\\ c_{1,r+1}\mathbf{1} & \ldots & c_{r,r+1}\mathbf{1} & (c_{r+1,r+1}-c_{r+1,r+2})I_{p-r}+c_{r+1,r+2}\mathbf{1}\mathbf{1}^{\rm T}\end{pmatrix} \tag{78}$$

where $\mathbf{1}=(1,\ldots,1)^{\rm T}$.

From the definition of $\mathbb{S}^{p-1}$,

$$\sum_{i=1}^p x_i^2=1. \tag{79}$$

Taking the expectation of equation (79) gives

$$\sum_{i=1}^r \lambda_i+(p-r)\lambda=1. \tag{80}$$

Multiplying equation (79) by x_j^2 and taking the expectation gives

$$\sum_{i=1}^r c_{ji}+(p-r)c_{j,r+1}=\lambda_j, \qquad j=1,\ldots,r. \tag{81}$$

Similarly, multiplying equation (79) by x_{r+1}^2 and taking the expectation gives

$$\sum_{j=1}^r c_{r+1,j}+c_{r+1,r+1}+(p-r-1)c_{r+1,r+2}=\lambda. \tag{82}$$

Further,

$$\begin{aligned}\big[(\cos\theta)x_r+(\sin\theta)x_{r+1}\big]^4 &= (\cos\theta)^4x_r^4+4(\cos\theta)^3(\sin\theta)x_r^3x_{r+1}\\ &\quad+6(\cos\theta)^2(\sin\theta)^2x_r^2x_{r+1}^2\\ &\quad+4(\cos\theta)(\sin\theta)^3x_rx_{r+1}^3+(\sin\theta)^4x_{r+1}^4,\end{aligned} \tag{83}$$

and so

$$\begin{aligned}c_{rr} &= (\cos\theta)^4c_{rr}+0+6(\cos\theta)^2(\sin\theta)^2c_{r,r+1}+0+(\sin\theta)^4c_{rr}\\ &= (\cos^2\theta+\sin^2\theta)^2c_{rr}+2\cos^2\theta\sin^2\theta(3c_{r,r+1}-c_{rr}), \quad \forall\theta,\end{aligned} \tag{84}$$

leading to

$$c_{rr}=3c_{r,r+1}. \tag{85}$$

Substituting equations (80), (81) and (85) into (82) yields

$$\sum_{j=1}^r\frac{1}{p-r}\left(\lambda_j-\sum_{i=1}^r c_{ij}\right)+(p-r+2)c_{r,r+1}=\frac{1-\sum_{i=1}^r\lambda_i}{p-r}, \tag{86}$$

and so

$$c_{r,r+1}=\frac{1-2\sum_{i=1}^r\lambda_i+\sum_{i=1}^r\sum_{j=1}^r c_{ij}}{(p-r)(p-r+2)}. \tag{87}$$

Simple calculations show that $(t_{r+1,r+1},\ldots,t_{pp};\ t_{r+1,r+2},\ldots,t_{p-1,p})^{\rm T}$ has variance matrix

$$\begin{bmatrix}(c_{r+1,r+1}-c_{r+1,r+2})I_{p-r}+(c_{r+1,r+2}-\lambda^2)\mathbf{1}\mathbf{1}^{\rm T} & \mathbf{0}\\ \mathbf{0} & c_{r+1,r+2}I_{(p-r)(p-r-1)/2}\end{bmatrix}. \tag{88}$$

It follows from equation (85) that this is equal to

$$c_{r+1,r+2}\begin{bmatrix}2I_{p-r}+(1-\lambda^2/c_{r+1,r+2})\mathbf{1}\mathbf{1}^{\rm T} & \mathbf{0}\\ \mathbf{0} & I_{(p-r)(p-r-1)/2}\end{bmatrix}. \tag{89}$$

Partition $\overline{T}=(\overline{t}_{ij})$ (according to the subspaces spanned by $\mu_1,\ldots,\mu_r$ and $\mu_{r+1},\ldots,\mu_p$, respectively) as

$$\overline{T}=\begin{pmatrix}\overline{T}_{11} & \overline{T}_{12}\\ \overline{T}_{21} & \overline{T}_{22}\end{pmatrix}, \tag{90}$$

where

$$\overline{T}_{11} = \begin{pmatrix} \bar{t}_{11} & \dots & \bar{t}_{1r} \\ \vdots & \ddots & \vdots \\ \bar{t}_{r1} & \dots & \bar{t}_{rr} \end{pmatrix} \tag{91}$$

and

$$\overline{T}_{22} = \begin{pmatrix} \bar{t}_{r+1,r+1} & \dots & \bar{t}_{r+1,p} \\ \vdots & \ddots & \vdots \\ \bar{t}_{p,r+1} & \dots & \bar{t}_{p,p} \end{pmatrix}. \tag{92}$$

Since the unit eigenvectors of $\overline{T}$ are $O(n^{-1/2})$ close to $\mu_1, \ldots, \mu_p$, we have

$$\left\| \overline{T}_{22} - \frac{\mathrm{tr}(\overline{T}_{22})}{p-r} I_{p-r} \right\|^2 = \sum_{i=r+1}^{p} (\bar{t}_i - \bar{t}_{\cdot 1})^2 + 2 \sum_{r+1 \le i < j \le p} \bar{t}_{ij}^2 + O(n^{-1/2}), \tag{93}$$

where $\bar{t}_1, \ldots, \bar{t}_p$ denote the eigenvalues of $\overline{T}$ and $\bar{t}_{\cdot 1} = \mathrm{tr}(\overline{T}_{22})/(p-r)$. It follows from equation (89) and the Proposition at the beginning of this appendix that

$$\frac{1}{2c_{r+1,r+2}} \left\| \overline{T}_{22} - \frac{\mathrm{tr}(\overline{T}_{22})}{p-r} I_{p-r} \right\|^2 \dot{\sim} \chi^2_{(p-r-1)(p-r+2)/2}, \quad n \to \infty. \tag{94}$$

From equation (87), a suitable estimate of $c_{r+1,r+2}$ is

$$\hat{c}_{r+1,r+2} = \frac{1 - 2\sum_{i=1}^{r} \hat{\lambda}_i + \sum_{i=1}^{r} \sum_{j=1}^{r} \hat{c}_{ij}}{(p-r)(p-r+2)}, \tag{95}$$

where

$$\begin{aligned} &\hat{\lambda}_i = \bar{t}_i, && i = 1, \ldots, r, \\ &\hat{c}_i j = \tfrac{1}{n} \sum_{k=1}^{n} (x_k^{\mathsf{T}} t_i)^2 (x_k^{\mathsf{T}} t_j)^2, && i, j = 1, \ldots, r, \end{aligned} \tag{96}$$

with $t_1, \ldots, t_p$ being the unit eigenvectors of $\overline{T}$.

A3.1. The case r = 0. This gives Bingham's (1974) test of uniformity (see p. 232 of Mardia & Jupp, 2000). Uniformity is rejected for large values of

$$\frac{p(p+2)}{2} n \| \overline{T} - p^{-1} I_p \|^2 = \frac{p(p+2)}{2} n \left(\sum_{i=1}^{p} \bar{t}_i^2 - \frac{1}{p} \right), \tag{97}$$

where $\bar{t}_1, \ldots, \bar{t}_p$ denote the eigenvalues of $\overline{T}$. Under uniformity,

$$\frac{p(p+2)}{2} n \left(\sum_{i=1}^{p} \bar{t}_i^2 - \frac{1}{p} \right) \dot{\sim} \chi^2_{(p+2)(p-1)/2}, \quad n \to \infty. \tag{98}$$

A3.2. The case r = 1. This gives Prentice's (1984) test of symmetry about an axis (see p. 235 of Mardia & Jupp, 2000). Symmetry about the major axis μ_1 is rejected for large values of

$$\frac{1}{2\hat{c}_{23}} \left\| \overline{T}_{22} - \frac{\mathrm{tr}(\overline{T}_{22})}{p-1} I_{p-1} \right\|^2 = \frac{n(p^2-1)[\sum_{i=2}^{p} \bar{t}_i^2 - (1-\bar{t}_1)^2/(p-1)]}{2(1 - 2\bar{t}_1 + \hat{c}_{11})}, \tag{99}$$

where $\bar{t}_1, \ldots, \bar{t}_p$ (with $\bar{t}_1 \ge \cdots \ge \bar{t}_p$) denote the eigenvalues of $\overline{T}$ corresponding to eigenvectors $t_1, \ldots, t_p$ and

$$\hat{c}_{11} = \frac{1}{n} \sum_{i=1}^{n} (x_i^{\mathsf{T}} t_1)^4. \tag{100}$$

Under symmetry,

$$\frac{n(p^2-1)[\sum_{i=2}^{p} \bar{t}_i^2 - (1-\bar{t}_1)^2/(p-1)]}{2(1 - 2\bar{t}_1 + \hat{c}_{11})} \dot{\sim} \chi^2_{(p+1)(p-2)/2}, \quad n \to \infty. \tag{101}$$

Similarly, symmetry about the minor axis μ_p is rejected for large values of

$$\frac{1}{2\hat{c}_{23}} \left\| \overline{T}_{22} - \frac{\mathrm{tr}(\overline{T}_{22})}{p-1} I_{p-1} \right\|^2 = \frac{n(p^2-1)[\sum_{i=1}^{p-1} \bar{t}_i^2 - (1-\bar{t}_p)^2/(p-1)]}{2(1 - 2\bar{t}_p + \hat{c}_{pp})}, \tag{102}$$

where

$$\hat{c}_{pp} = \frac{1}{n} \sum_{i=1}^{n} (x_i^{\mathsf{T}} t_p)^4. \tag{103}$$

Under symmetry,

$$\frac{n(p^2-1)[\sum_{i=1}^{p-1} \bar{t}_i^2 - (1-\bar{t}_p)^2/(p-1)]}{2(1 - 2\bar{t}_p + \hat{c}_{pp})} \dot{\sim} \chi^2_{(p+1)(p-2)/2}, \quad n \to \infty. \tag{104}$$

A3.3. The case r = 2. We consider the prolate and oblate cases in turn.

(*a*) Prolate case

$O(p-2)$ symmetry of the distribution about the plane spanned by μ_1 and μ_2 is rejected for large values of

$$\frac{1}{2\hat{c}_{34}} \left\| \overline{T}_{22} - \frac{\mathrm{tr}(\overline{T}_{22})}{p-2} I_{p-2} \right\|^2 = \frac{np(p-2)[\sum_{i=3}^{p} \bar{t}_i^2 - (1-\bar{t}_1-\bar{t}_2)^2/(p-2)]}{2[1 - 2(\bar{t}_1+\bar{t}_2) + \hat{c}_{11} + 2\hat{c}_{12} + \hat{c}_{22}]}, \tag{105}$$

where $\bar{t}_1, \ldots, \bar{t}_p$ (with $\bar{t}_1 \ge \cdots \ge \bar{t}_p$) denote the eigenvalues of $\overline{T}$ corresponding to eigenvectors $t_1, \ldots, t_p$ and

$$\hat{c}_{ij} = \frac{1}{n} \sum_{k=1}^{n} \left(x_k^{\mathsf{T}} t_i \right)^2 \left(x_k^{\mathsf{T}} t_j \right)^2. \tag{106}$$

Under symmetry,

$$\frac{np(p-2)[\sum_{i=3}^{p} \bar{t}_i^2 - (1-\bar{t}_1-\bar{t}_2)^2/(p-2)]}{2[1 - 2(\bar{t}_1+\bar{t}_2) + \hat{c}_{11} + 2\hat{c}_{12} + \hat{c}_{22}]} \dot{\sim} \chi^2_{p(p-3)/2}, n \to \infty, \tag{107}$$

and this statistic is asymptotically equal to w_{prolate} of equation (69).

(*b*) Oblate case

Similarly, $O(p-2)$ symmetry of the distribution about the plane spanned by μ_1 and μ_p is rejected for large values of

$$\frac{1}{2\hat{c}_{23}}\left\|\overline{T}_{22}-\frac{\mathrm{tr}(\overline{T}_{22})}{p-2}I_p-2\right\|^2=\frac{np(p-2)[\sum_{i=2}^{p-1}\bar{t}_i^2-(1-\bar{t}_1-\bar{t}_p)^2/(p-2)]}{2[1-2(\bar{t}_1+\bar{t}_p)+\hat{c}_{11}+2\hat{c}_{1p}+\hat{c}_{pp}]}. \quad (108)$$

Under symmetry,

$$\frac{np(p-2)[\sum_{i=2}^{p-1}\bar{t}_i^2-(1-\bar{t}_1-\bar{t}_p)^2/(p-2)]}{2[1-2(\bar{t}_1+\bar{t}_p)+\hat{c}_{11}+2\hat{c}_{1p}+\hat{c}_{pp}]}\stackrel{\cdot}{\sim}\chi^2_{p(p-3)/2},\ n\to\infty, \quad (109)$$

and this statistic is asymptotically equal to w_{oblate} of equation (70).

APPENDIX *B*
Computations and asymptotics

B1. Numerical computations

In order to solve the nonlinear equation (36) we used a modified Newton method. For brevity we write this equation as $f(\kappa)=\lambda$, with $\kappa=(\kappa_1,\kappa_2,\kappa_3,\kappa_4)$ and $\lambda=(\lambda_1,\lambda_2,\lambda_3,\lambda_4)$.

Recall that a solution exists only if $0<\lambda_j<1$ $(j=1,2,3,4)$ and $\sum_1^4\lambda_j=1$, and then $\kappa_1,\kappa_2,\kappa_3,\kappa_4$ are determined up to an additive constant. This implies that the Jacobian Df of f is not invertible, and thus we modified Newton's method by using the pseudo-inverse of Df. The initial values for Newton's iteration were chosen according to equation (38), *i.e.*

$$\tilde{\kappa}_1=0,\quad \tilde{\kappa}_j=-(2\lambda_j)^{-1}\quad (j=2,3,4). \quad (110)$$

During the computations the approximate solutions were normalized such that $\sum_1^4\kappa_j=0$.

The Jacobian Df involves not only the hypergeometric function ${}_1F_1(1/2;2;K)$ but also its first and second derivatives. When we performed the experiments we were not aware of the Kume–Wood formula (Kume & Wood, 2007), which expresses the derivatives of ${}_1F_1(1/2;2;K)$ by the values of a higher-dimensional hypergeometric function, and thus we approximated the derivatives numerically.

The range of λ we were mainly interested in is

$$1-3\varepsilon\le\lambda_1<1,\qquad 0<\lambda_2,\lambda_3,\lambda_4\le\varepsilon, \quad (111)$$

with small ε. In this range the function f is rather flat. For example, at $\lambda=(1-3\varepsilon,\varepsilon,\varepsilon,\varepsilon)$ we observed the asymptotic behaviour

$$Df\simeq\frac{1}{2\varepsilon^2}\begin{pmatrix}3&-1&-1&-1\\-1&1&0&0\\-1&0&1&0\\-1&0&0&-1\end{pmatrix} \quad (112)$$

as $\varepsilon\to+0$. In practice, computations had to be performed in the range of κ_j between -1000 and 1000. Since it was impossible to meet the required accuracy with existing *Matlab* code (we are grateful to Raymond Kan) we transferred parts of this code into *Mathematica* (Wolfram Research, Champaign, IL, USA) and used high-precision arithmetic.

Note that, in the present case of highly concentrated distributions, it may be advantageous to evaluate ${}_1F_1(1/2;2;K)$ using the asymptotic formula, equation (9) of Bingham *et al.* (1992), for the normalizing constant of concentrated Bingham distributions, which gives for $p=1,2,\ldots$

$$\begin{aligned}{}_1F_1(1/2;2;A)&=\exp(\kappa_1)\pi^{-1/2}|T_0|^{-1/2}\,{}_2F_0\big(1/2;1/2;T_0^{-1}\big)\\&=\exp(\kappa_1)\pi^{-1/2}|T_0|^{-1/2}\\&\quad\times\left\{\sum_{k=0}^{p-1}\frac{[(1/2)_k]^2C_{(k)}(T_0^{-1})}{k!}+\mathrm{O}(\tau^{-p})\right\}\end{aligned} \quad (113)$$

as $\tau\to\infty$, where $\kappa_1,\ldots,\kappa_4$ are the eigenvalues (assumed to be distinct) of A, $T_0=\mathrm{diag}(\kappa_1-\kappa_2,\kappa_1-\kappa_3,\kappa_1-\kappa_4)$, $C_{(k)}$ is the top-order zonal polynomial corresponding to the single-element partition of k, and $\tau=\min(\kappa_1-\kappa_2,\kappa_1-\kappa_3,\kappa_1-\kappa_4)$. Here it is assumed that $\kappa_1,\kappa_2,\kappa_3,\kappa_4$ are distinct; an extension to the general case is given in Appendix 2 of Bingham *et al.* (1992).

Taking $\kappa_1=0$ (which we may do without loss of generality) and $p=2$ gives

$${}_1F_1(1/2;2;A)=\pi^{-1/2}(-\kappa_2\kappa_3\kappa_4)^{-1/2}\left[1-\frac{1}{2}\sum_{j=2}^4\frac{1}{\kappa_j}+\mathrm{O}(\tau^{-2})\right]. \quad (114)$$

Then

$$\frac{\partial_1F_1(1/2;2;A)}{\partial\kappa_j}=-\frac{1}{2\kappa_j}+\frac{1}{2\kappa_j{}^2}+\mathrm{O}(\tau^{-3}),\qquad j=2,3,4. \quad (115)$$

Combining equation (115) with equation (36) shows that the maximum likelihood estimates $\hat{\kappa}_2,\hat{\kappa}_3$ and $\hat{\kappa}_4$ of κ_2,κ_3 and κ_4 satisfy

$$\lambda_j=-\frac{1}{2\hat{\kappa}_j}\left(1-\frac{1}{\hat{\kappa}_j}\right)+\mathrm{O}(\tau^{-3}),\qquad j=2,3,4. \quad (116)$$

Hence

$$\hat{\kappa}_j\left(1-\frac{1}{\hat{\kappa}_j}\right)^{-1}=-\frac{1}{2\lambda_j}+\mathrm{O}(\tau^{-1}),\qquad j=2,3,4, \quad (117)$$

and so

$$\hat{\kappa}_j+1=-\frac{1}{2\lambda_j}+\mathrm{O}(\tau^{-1}),\qquad j=2,3,4. \quad (118)$$

Define $\check{\kappa}_2,\check{\kappa}_3$ and $\check{\kappa}_4$ by

$$\check{\kappa}_j=-\frac{1}{2\lambda_j}-1,\qquad j=2,3,4. \quad (119)$$

Then equation (118) shows that

$$\check{\kappa}_j=\hat{\kappa}_j+\mathrm{O}(\tau^{-1}),\qquad j=2,3,4. \quad (120)$$

From $\sum_{j=1}^4\lambda_j=1$ and equation (116) we have

$$\lambda_1=1+\sum_{j=2}^4\frac{1}{2\hat{\kappa}_j}\left(1-\frac{1}{\hat{\kappa}_j}\right)+\mathrm{O}(\tau^{-3}), \quad (121)$$

so that

$$\frac{1}{2\lambda_1} = \frac{1}{2} - \frac{1}{4}\sum_{j=2}^{4}\frac{1}{\hat{\kappa}_j} + \mathrm{O}(\tau^{-2}). \tag{122}$$

Setting

$$\tilde{\kappa}_1 = 0, \quad \tilde{\kappa}_j = -(2\lambda_j)^{-1} - (2\lambda_1)^{-1}, \quad j = 2, 3, 4, \tag{123}$$

and combining equation (122) with equation (118) gives

$$\tilde{\kappa}_j = -\frac{1}{2\lambda_j} - \frac{1}{2\lambda_1} = \hat{\kappa}_j + \frac{1}{2} + \mathrm{O}(\tau^{-1}), \quad j = 2, 3, 4. \tag{124}$$

Let $\mathring{\kappa}_2, \mathring{\kappa}_3$ and $\mathring{\kappa}_4$ be the estimators [motivated by the arguments leading to equation (38) and given in equation (110)] defined by

$$\mathring{\kappa}_j = -\frac{1}{2\lambda_j}, \qquad j = 2, 3, 4. \tag{125}$$

Combining equations (120), (124), (125) and (119) gives

$$\begin{aligned} \check{\kappa}_j &= \hat{\kappa}_j + \mathrm{O}(\tau^{-1}), \\ \tilde{\kappa}_j &= \hat{\kappa}_j + \frac{1}{2} + \mathrm{O}(\tau^{-1}), \\ \mathring{\kappa}_j &= \hat{\kappa}_j + 1 + \mathrm{O}(\tau^{-1}). \end{aligned} \tag{126}$$

Thus, for concentrated distributions, $\check{\kappa}_j$ will tend to be closer to $\hat{\kappa}_j$ than $\tilde{\kappa}_j$ is, which in turn will tend to be closer to $\hat{\kappa}_j$ than $\mathring{\kappa}_j$ is.

B2. Asymptotic formulae

In order to check the quality of the approximation equation (44) we did 1000 tests with randomly chosen values of λ in the range given by equation (111), computed the corresponding approximate values $\tilde{\kappa}$ by equation (44) and checked the corresponding values $\tilde{\lambda} = f(\tilde{\kappa})$ against λ. Since we are only interested in λ_j and κ_j for $j = 2, 3, 4$, we measure the discrepancy in terms of the absolute and relative errors

$$\Delta\lambda = \max|\tilde{\lambda}_j - \lambda_j|, \qquad \delta\lambda = \frac{\max|\tilde{\lambda}_j - \lambda_j|}{\max|\lambda_j|}. \tag{127}$$

For $\varepsilon = 0.003$ (which was satisfied for the data in Table 1) we obtained the upper bounds $\Delta\lambda < 0.000041$, $\delta\lambda < 0.015$, and for $\varepsilon = 0.01$ we still had $\Delta\lambda < 0.00058$, $\delta\lambda < 0.058$.

Moreover, we confirmed empirically that the solution to equation (36) is even better approximated by equation (123) instead of equation (110). Here 1000 random tests with $\varepsilon = 0.003$ gave $\Delta\lambda < 1.5 \times 10^{-7}$, $\delta\lambda < 5.0 \times 10^{-5}$, for $\varepsilon = 0.01$ we obtained $\Delta\lambda < 6.1 \times 10^{-6}$, $\delta\lambda < 6.1 \times 10^{-4}$, and even for $\varepsilon = 0.1$ the estimated errors were $\Delta\lambda < 0.0076$, $\delta\lambda < 0.092$.

Since the test statistics [equations (39), (42), (43)] involve only differences of $\kappa_2, \kappa_3, \kappa_4$ and $\lambda_2, \lambda_3, \lambda_4$, which are not influenced by the additional term $(2\lambda_1)^{-1}$ in equation (123), we obtain the same approximations [equations (45), (46), (47)] also for the modified values of κ_j. Thus treating our experimental data with the simple approximate formulae [equation (110)] amounts to a smaller effect than perturbing the measured values of λ by 0.005%.

Special thanks are due to Raymond Kan and Joseph L. Rotman of the School of Management, University of Toronto, Ontario, Canada, for contributing a *Matlab* script file to evaluate ${}_1F_1(1/2; 2; K)$, and to Plamen Koev, Department of Mathematics, San Jose State University, CA, USA, for introducing us to Raymond Kan and pointing out the particularly simple form of ${}_1F_1(1/2; 2; K)$ in terms of top-order zonal polynomials (*cf.* Hillier *et al.*, 2009; Koev & Edelman, 2006). WP gratefully acknowledges the Danish National Research Foundation for supporting the Center for Fundamental Research: Metal Structures in Four Dimensions, within which part of this work was performed. HS would like to thank Fundação Coordenação de Aperfeiçoamento de Pessoal de Nível (CAPES) and the German Academic Exchange Service (DAAD) for funding a three-month research stay at Centro de Microscopia da Universidade Federal de Minas Gerais in Belo Horizonte, Brazil, during which time this paper was completed. All authors would like to thank David Mainprice, Géosciences UMR CNRS 5243, Université Montpellier 2, for his insightful and constructive review which helped to clarify and improve our communication.

References

Barton, N. R. & Dawson, P. R. (2001*a*). *Mater. Sci. Eng.* **9**, 433–463.
Barton, N. R. & Dawson, P. R. (2001*b*). *Metall. Mater. Trans.* **32**, 1967–1975.
Bingham, C. (1964). PhD thesis, Yale University, USA, p. 80.
Bingham, C. (1974). *Ann. Stat.* **2**, 1201–1225.
Bingham, C., Chang, T. & Richards, D. (1992). *J. Mult. Anal.* **41**, 314–337.
Bonham-Carter, G. F. (1996). *Geographic Information Systems for Geoscientists.* Oxford: Pergamon Press.
Boogaart, K. G. van den (1999). *Proceedings of the Twelfth International Conference on Textures of Materials* (ICOTOM-12), August 9–13, 1999, Montreal, Quebec, Canada, edited by J. A. Szpunar, Vol. 1, pp. 29–33. Ottawa: NRC Research Press.
Boogaart, K. G. van den (2002). PhD thesis, Technische Universität Freiberg, Germany. Aachen: Shaker-Verlag.
Boogaart, K. G. van den & Schaeben, H. (2002*a*). *Math. Geol.* **34**, 479–503.
Boogaart, K. G. van den & Schaeben, H. (2002*b*). *Math. Geol.* **34**, 671–677.
Cho, J.-H., Rollett, A. D. & Oh, K. H. (2005). *Metall. Mater. Trans. A*, **36**, 3427–3438.
El-Dasher, B. S., Adams, B. L. & Rollett, A. D. (2003). *Scr. Mater.* **48**, 141–145.
Field, D. P., Trivedi, P. B., Wright, S. I. & Kumar, M. (2005). *Ultramicroscopy*, **103**, 33–39.
Glez, J. C. & Driver, J. (2001). *J. Appl. Cryst.* **34**, 280–288.
Gürlebeck, K., Habetha, K. & Sprössig, W. (2006). *Funktionentheorie in der Ebene und im Raum.* Basel, Boston, Berlin: Birkhäuser.
He, W., Ma, W. & Pantleon, W. (2008). *Mater. Sci. Eng. A*, **494**, 21–27.
Heilbronner, R. (2000). *J. Struct. Geol.* **22**, 969–981.
Hielscher, R. (2007). PhD thesis, TU Bergakademie Freiberg, Germany.
Hielscher, R. & Schaeben, H. (2008). *J. Appl. Cryst.* **41**, 1024–1037.
Hillier, G., Kan, R. & Wang, X. (2009). *Econom. Theor.* **25**, 211–242.
Humbert, M., Gey, N., Muller, J. & Esling, C. (1996). *J. Appl. Cryst.* **29**, 662–666.
Humphreys, F. J., Bate, P. S. & Hurley, P. J. (2001). *J. Microsc.* **201**, 50–58.
Koev, P. & Edelman, A. (2006). *Math. Comput.* **75**, 833–846.
Krog-Pedersen, S., Bowen, J. R. & Pantleon, W. (2009). *Int. J. Mater. Res.* pp. 433–438.

Kume, A. & Wood, A. T. A. (2007). *Stat. Probab. Lett.* **77**, 832–837.
Kunze, K. & Schaeben, H. (2004). *Math. Geol.* **36**, 917–943.
Kunze, K. & Schaeben, H. (2005). *Mater. Sci. Forum*, **495–497**, 295–300.
Lloyd, G. E., Farmer, A. B. & Mainprice, D. (1997). *Tectonophysics*, **279**, 55–78.
Mardia, K. V. & Jupp, P. E. (2000). *Directional Statistics.* Chichester: J. Wiley and Sons.
Morawiec, A. (1998). *J. Appl. Cryst.* **31**, 818–819.
Nye, J. F. (1953). *Acta Metall.* **1**, 153–162.
Pantleon, W. (2005). *Mater. Sci. Technol.* **21**, 1392–1396.
Pantleon, W. (2008). *Scr. Mater.* **58**, 994–997.
Pantleon, W., He, W., Johansson, T. P. & Gundlach, C. (2008). *Mater. Sci. Eng. A*, **483–484**, 668–671.
Prentice, M. J. (1984). *Biometrika*, **71**, 147–154.
Prentice, M. J. (1986). *J. R. Stat. Soc. Ser. B*, **48**, 214–222.
Schaeben, H. (1993). *J. Appl. Cryst.* **26**, 112–121.
Schaeben, H., Hielscher, R., Fundenberger, J.-J., Potts, D. & Prestin, J. (2007). *J. Appl. Cryst.* **40**, 570–579.
Watson, G. S. (1983). *Statistics on Spheres.* New York: J. Wiley and Sons.
Wheeler, J., Mariani, E., Piazolo, S., Prior, D. J., Trimby, P. & Drury, M. R. (2009). *J. Microsc.* **233**, 482–494.
Wilkinson, A. J., Meaden, G. & Dingley, D. J. (2006). *Mater. Sci. Technol.* **22**, 1271–1278.